General Disclaimer

One or more of the Following Statements may affect this Document

- This document has been reproduced from the best copy furnished by the organizational source. It is being released in the interest of making available as much information as possible.

- This document may contain data, which exceeds the sheet parameters. It was furnished in this condition by the organizational source and is the best copy available.

- This document may contain tone-on-tone or color graphs, charts and/or pictures, which have been reproduced in black and white.

- This document is paginated as submitted by the original source.

- Portions of this document are not fully legible due to the historical nature of some of the material. However, it is the best reproduction available from the original submission.

Produced by the NASA Center for Aerospace Information (CASI)

X-716-66-473

NASA TM X- 55641

A FUNCTIONALLY-INTEGRATED CONTROLLER-COMMUTATOR FOR USE IN BRUSHLESS DIRECT-DRIVE SOLAR ARRAY REORIENTATION SYSTEMS

BY

L.J. VEILLETTE

GPO PRICE $ _____

CFSTI PRICE(S) $ 3.00

Hard copy (HC) _____

Microfiche (MF) .65

ff 653 July 65

SEPTEMBER 1966

NASA — GODDARD SPACE FLIGHT CENTER

GREENBELT, MARYLAND

N67 16544

(ACCESSION NUMBER) (THRU)

54 1

(PAGES) (CODE)

TMX-55641 03

(NASA CR OR TMX OR AD NUMBER) (CATEGORY)

FACILITY FORM 602

X-716-66-473

A FUNCTIONALLY-INTEGRATED CONTROLLER-COMMUTATOR FOR USE IN BRUSHLESS DIRECT-DRIVE SOLAR ARRAY REORIENTATION SYSTEMS

by

L. J. Veillette

September 1966

Goddard Space Flight Center
Greenbelt, Maryland

PRECEDING PAGE BLANK NOT FILMED.

CONTENTS

ILLUSTRATIONS

A FUNCTIONALLY-INTEGRATED CONTROLLER-COMMUTATOR FOR USE IN BRUSHLESS DIRECT-DRIVE SOLAR ARRAY REORIENTATION SYSTEMS

by

L. J. Veillette

ABSTRACT

This report presents solutions to some of the specialized problems arising in the design of a brushless, direct-drive solar array reorientation system. Specifically, a simple active magnetic sensing method is described which derives position and rate information directly from the solar array output shaft. The angular resolution and rate-sensitivity available from the sensor are suitable for providing controlled-damping and rate-limiting of the solar array at orbital rates. The sensor rate sensing capability is integrated into the commutator simply by appropriately selecting the geometric proportions of the sensor magnetic structure. Expressions derived for the sensor gain, bandwidth, and driving-point impedances show that increase of the sensor minimum bandwidth is obtained at the expense of increased input drive requirements, reduced low-frequency gain, or reduced output loading.

Bidirectional drive of the solar array is obtained in a single sensor by employing a phase-controlled logic technique to establish the torque motor armature switching sequences. Boolean excitation and connection matrices and winding vectors for implementing the logical design are derived. Torque/speed control using excitation-level modulation or pulse-modulation of the torque motor armature current are integrated into the commutator with practically no penalty in added circuit complexity. The solution to these problems in integrated form yields a simpler overall solar array drive system design with correspondingly improved reliability.

ACKNOWLEDGEMENTS

The successful completion of this work has been possible only with the support of many persons. In particular I wish to express my appreciation for project support given by Messrs. F. C. Yagerhofer and W. R. Cherry of GSFC Space Power Technology Branch, and Mr. P. T. Maxwell of NASA Headquarters. I wish also to acknowledge the valuable assistance of Messrs. S. R. Williams and R. L. Baker in conducting the earlier phases of the laboratory work, and Messrs. W. Hardisty and R. Nottingham for the later test work. Earlier sensor work by Mr. W. W. Yates of Westinghouse Electric Corporation (reference 1) has also been helpful.

A FUNCTIONALLY-INTEGRATED CONTROLLER-COMMUTATOR FOR USE IN BRUSHLESS DIRECT-DRIVE SOLAR ARRAY REORIENTATION SYSTEMS

I. INTRODUCTION

Orientation of solar power arrays on many earth-orbiting spacecraft requires that a drive mechanism be provided to continuously point the array toward the sun. It is necessary that part or all of the drive system operate in the vacuum of outer space where gear and bearing lubrication problems, and brush and commutator friction and wear, substantially reduce the reorientation system life and reliability. It is desirable, therefore, that the required solar array orientation be provided in a system in which gears, gear-support bearings, slip-rings, brush and commutator assemblies, and sealed chambers (through which mechanical power must be transmitted) are eliminated. These purposes are achieved in a brushless, direct-drive solar array reorientation system presently being developed at GSFC. Implementation of this system concept has required three essential subsystem developments as follows: (1) a brushless D/C torque motor with magnetically-actuated commutator[1], (2) a brushless power transfer means that is effectively integrated into the power conditioning system[2], and (3) a brushless rate-sensing method with sufficient sensitivity to provide controlled-damping and rate-limiting of the solar array at orbital rates. Portions of the subsystem work have been completed on NASA contracts cited in references 1 and 2. This report presents the design of the electronic commutation and rate-sensing portions of the reorientation system into which the torque/speed control and bidirectional drive functions are integrated.

Implementation of the functionally-integrated controller-commutator concept presented in this report has necessitated development of new designs leading to several invention disclosures. These are the phase-controlled logic technique, the integrated commutation and rate-sensing method, and the offset-tooth magnetic sensor configuration. The successful development of these techniques has resulted in a simple controller-commutator design capable of long-life and high reliability operation directly in the space environment.

II. CONTROLLER-COMMUTATOR OPERATION

The controller-commutator circuit commutates source power between three phases of the torque motor armature windings in a manner to maintain the motor

torque angle near the optimum value of 90 electrical degrees. The armature drive signals are dependent on the angular position of the rotor so that a rotor-position sensing function is required. This function is provided by a magnetic sensor that actuates a sequence of six armature switches connected in a three-phase bridge configuration. The magnetic sensor is active and operates on a variable reluctance principle, rather than as a PM device, so that useable signal levels are obtainable from the sensor when driving the solar array at orbital rates. The armature switches are driven regeneratively to avoid damage due to excessive heat dissipation when operating under stall conditions at or near the commutation points.

A number of the solar array control functions are integrated into the commutation circuitry. These are, integration of (1) the rate-sensing function of the controller into the rotor-position sensor of the commutator, (2) the bi-directional drive of the controller into the bridge network of the commutator using phase control of the sensor drive to provide the required logic in a single sensing element, and (3) the torque/speed control function of the controller into the regenerative drive circuitry of the commutator. A brief description of the controller-commutator circuit is given in the following.

A block diagram of the functionally-integrated controller-commutator is shown in Figure 1. It consists of circuits performing the following functions.

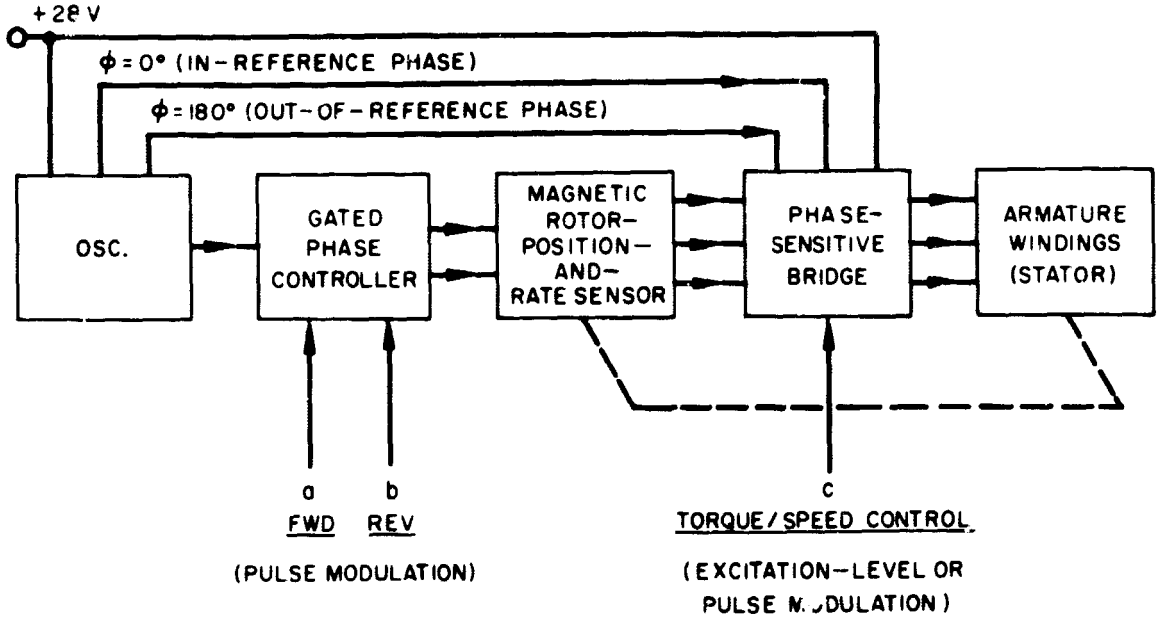

Figure 1–Block Diagram of Functionally-Integrated Controller-Commutator

Oscillator — converts 28 volt DC power to AC to drive the magnetic sensor, supplies reference-phase signals, and provides bias supplies to improve circuit design margins.

Gated Phase Controller — controls phase of the magnetic sensor signals by gating either at terminal "a" or terminal "b".

Magnetic Rotor-Position-and-Rate Sensor — provides three output signals differing in amplitude sequence and phase depending on the rotor angular position. The output signals provide 360° coverage of position and rate information derived directly from the solar array output shaft

Phase-Sensitive Bridge — provides regenerative amplification of the magnetic sensor signals, detects the phases of the sensor output signals, and modulates the duty-cycle of the lower-leg armature switches at terminal "c".

Armature Windings — produce torque motor armature field with either a delta or a wye connection.

A schematic diagram of the controller-commutator is given in Figure 2. The dashed lines divide the circuit into sections that show the implementation of each block in the diagram of Figure 1.

The controller-commutator is operated in the forward direction, $\dot{\theta} > 0$, by applying a +10 volt gating signal to terminal "a", Figures 1 and 2. The oscillator output then drives the magnetic sensor primary winding in-phase with the oscillator reference phase $\varphi = 0°$. The forward-direction amplitude sequences and phases of the three sensor outputs, V_1, V_2, V_3, are shown in Figure 3. The rise and fall or transition portions of the sensor output characteristic provide derived-rate information suitable for controlled-damping and rate-limiting of the solar array at orbital rates. The sensor signals actuate "magnetic core schmitt" circuits (designated MCS for purposes of this report) in each leg of a phase-sensitive bridge, Figure 4, and these circuits in turn drive the armature switches of A_1, A_2, A_3, B_1, B_2, B_3. Inhibit signals of phase $\varphi = 0°$ are applied to the bridge upper leg circuitry and inhibit signals of phase $\varphi = 180°$ are applied to the lower leg circuitry. A given armature switch is actuated when the sensor and inhibit signals applied to the corresponding MCS circuit are in-phase with each other and both are positive. Out-of-phase signals inhibit armature switch operation. The magnetic sensor signals depicted in Figure 3 establish the forward-direction torque sequence shown in Figure 5.

Reverse operation of the torque motor is achieved by reversing the phase of the magnetic sensor signals by gating the phase-controller at terminal "b",

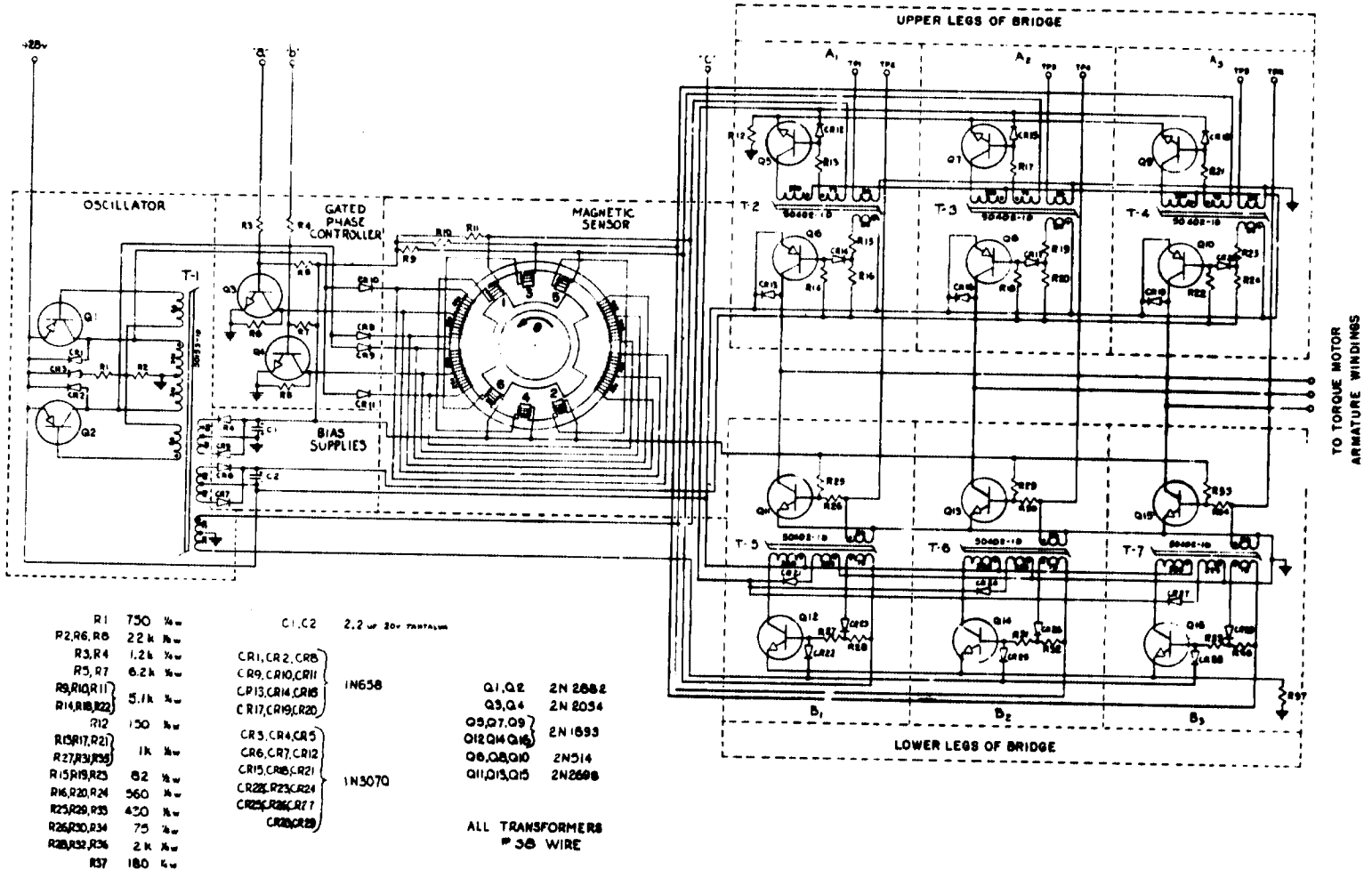

Figure 2–Schematic Dicgram of Functionally-Integrated Controller-Commutator

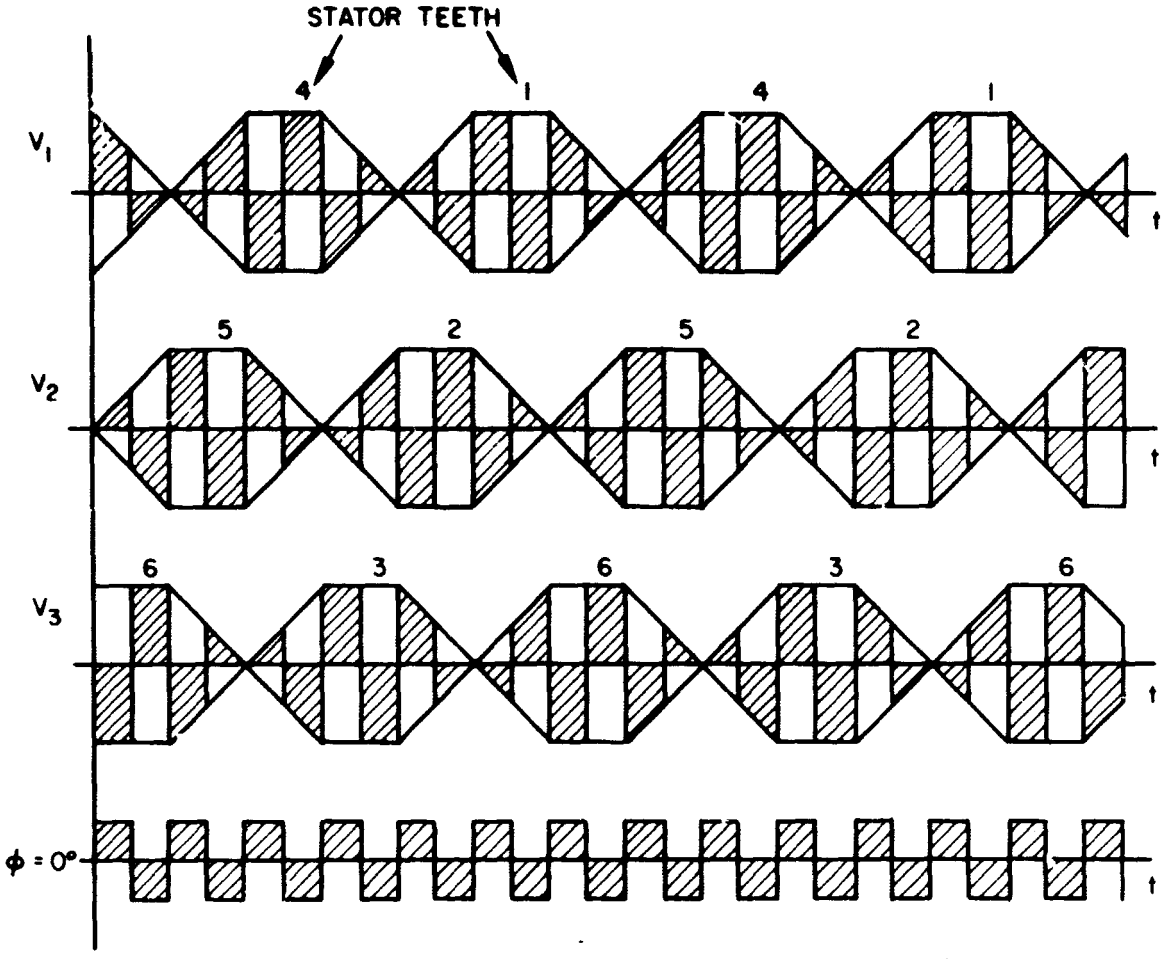

Figure 3–Magnetic Rotor-Position-and-Rate Sensor Output Signals (forward-direction amplitude sequence and phase) and Reference Phase $\phi = 0°$

Figures 1 and 2. Since the inhibit signals to the upper-leg circuits of the bridge are out-of-phase with the inhibit signals to the lower-leg circuits the roles of the upper-leg and lower-leg circuits are interchanged and the reverse-direction torque sequence of Figure 5 is produced.

Torque/speed control of the motor is achieved by varying the voltage at terminal "c", Figures 1 and 2, in the range from 0 to 12 volts. This voltage controls the rate of flux reset in the MCS circuits that drive the lower-leg armature switches of the bridge. The duty-cycle of the lower leg switches is thus varied resulting in pulse-width modulation of the excitation voltage applied to the torque motor winding. Since the period of oscillation is short compared to the torque motor winding time constant the windings filter out variations in the armature current so that excitation-level modulation control is achieved.

III. PHASE-CONTROLLED LOGIC

The purpose of this section of the report is to develop boolean excitation and connection matrices and sensor winding vectors necessary to implement the phase-controlled logic employed in the controller-commutator design. A significant feature of the result is the simplicity with which both forward and reverse direction armature switching sequences are obtained.

In the development undertaken in this section the torque motor armature windings are taken in a wye configuration with two-legs excited at a time from a 3-phase bridge circuit. A similar development can be made for delta winding configurations or wye configurations with alternately two-leg and three-leg excitation. The complex armature winding mmf, $\hat{F}_a$, is expressible in terms of the bridge circuit upper-leg switching states, A_m, the lower-leg switching states, B_n, and the successive rotor field positions, $(p - 1)\pi/3$, measured in electrical degrees, as follows,

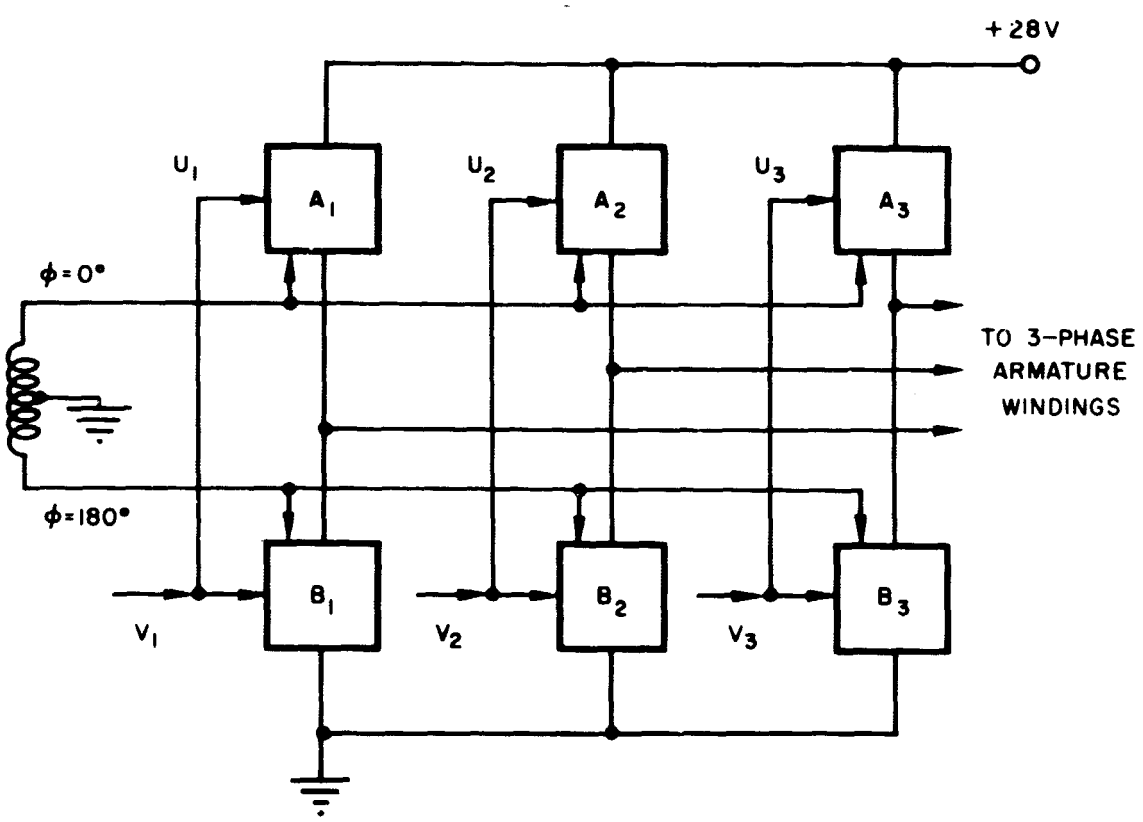

Figure 4–Phase-Sensitive Bridge

$$\hat{F}_a = - |\hat{F}_a| \left[\sum_m A_m \angle \left(\frac{2m}{3} - 1 \right) \pi - \sum_n B_n \angle \left(\frac{2n}{3} - 1 \right) \pi \right] \tag{1}$$

where

$$A_m = \begin{cases} 1, \; m = \alpha \equiv \dfrac{1}{4} \left[2p + 1 - (-1)^p \right] & \text{mod } 3 \\ & m = 1, 2, 3 \\ 0, \; m \neq \alpha & p = 1, 2, 3, \cdots \end{cases} \tag{2}$$

and

$$B_n = \begin{cases} 1, \; n = \beta \equiv p + 2 - \alpha, \text{ mod } 3, & n = 1, \; 2, \; 3 \\ & p = 1, \; 2, \; 3, \; \cdots \\ 0, \; n \neq \beta \end{cases} \tag{3}$$

for forward direction torquing, and where

$$A_m = \begin{cases} 1, \; m = \gamma \equiv p + 2 - \delta, \text{ mod } 3, & m = 1, \; 2, \; 3 \\ & p = 1, \; 2, \; 3, \; \cdots \\ 0, \; m \neq \gamma \end{cases} \tag{4}$$

and

$$B_n = \begin{cases} 1, \; n = \delta \equiv \dfrac{1}{4} \left[2p + 1 - (-1)^p \right], \text{ mod } 3, & \\ & n = 1, \; 2, \; 3 \\ 0, \; n \neq \delta & p = 1, \; 2, \; 3, \; \cdots \end{cases} \tag{5}$$

for reverse torquing. In the above expressions

$\equiv$ symbolizes a congruence[3] (modulus 3)

α = index of conducting upper-leg armature switch for forward-torquing sequence

β = index of conducting lower-leg armature switch for forward-torquing sequence

γ = index of conducting upper-leg armature switch for reverse-torquing sequence

δ = index of conducting lower-leg armature switch for reverse-torquing sequence

p = rotor field position index

The forward and reverse armature switching sequences corresponding to relations (2) thru (5) are given in Figure 5.

The upper-leg armature switches, A_m, are actuated by bridge input signals U_m that are in-reference phase and the lower-leg armature switches, B_n, are actuated by input signals V_n that are out-of-reference phase. We thus have the following logical expressions

$$A_m = R \cdot U_m + \Delta (R \cdot U_m), \; m = 1, \; 2, \; 3 \tag{7}$$

and

$$B_n = S \cdot V_n + \Delta (S \cdot V_n), \; n = 1, \; 2, \; 3 \tag{8}$$

where R is the in-reference square wave and equals logical 1 during the positive half-cycle and logical 0 during the negative half-cycle. S is the out-of-reference square wave and is also equal to logical 1 on the positive half-cycle and logical 0 on the negative half-cycle. Since R and S are 180° out of time phase it follows that

$$S = \overline{R} \tag{9}$$

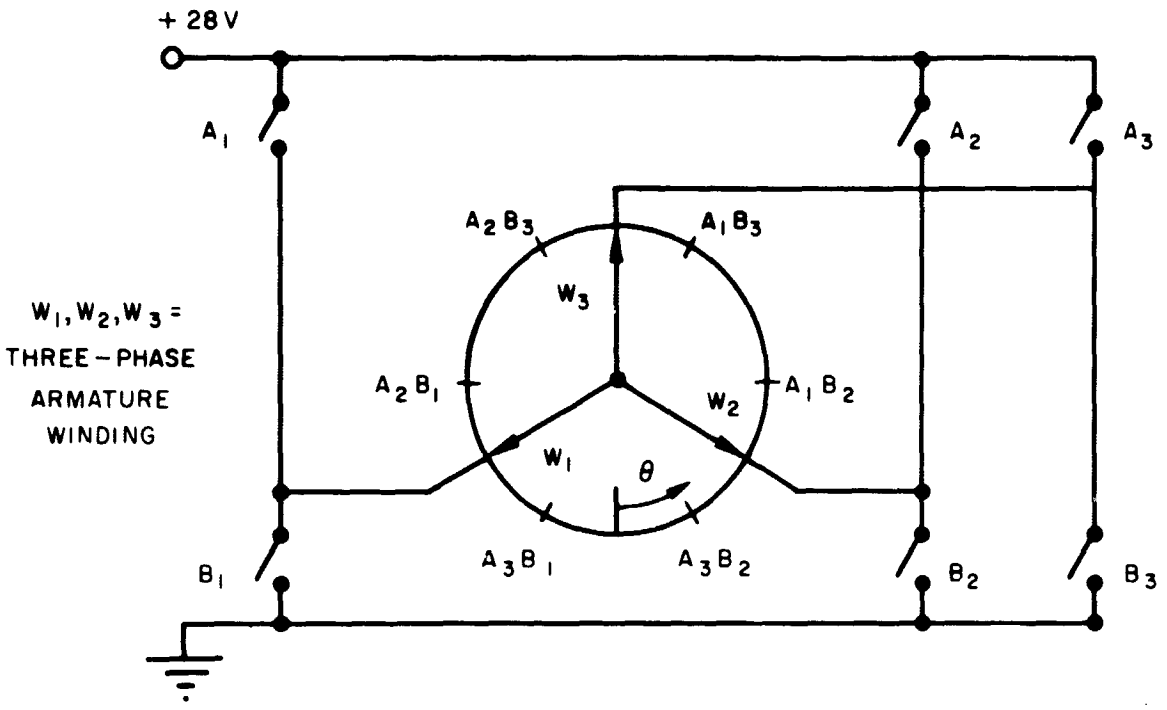

P	Rotor Field Angular Position	Forward-Direction Torque Sequence α	β	Reverse-Direction Torque Sequence γ	δ
1	$-30° < \theta < 30°$	1	2	2	1
2	$30° < \theta < 90°$	1	3	3	1
3	$90° < \theta < 150°$	2	3	3	2
4	$150° < \theta < 210°$	2	1	1	2
5	$210° < \theta < 270°$	3	1	1	3
6	$270° < \theta < 330°$	3	2	2	3
7	$330° < \theta < 390°$	1	2	2	1

Figure 5–Relation Between Torque Motor Field Position and Armature Switching Sequences for Optimum Torque Angle Over Angular Interval of 360 Electrical Degrees

at all instants of time. Thus the out-of-reference phase is designated $\bar{R}$. The half-cycle delay function, Δ, in equations (7) and (8) maintain the conducting armature switches driven on during the negative half-cycle of the actuating signal. Multiplying (7) by R and (8) by $S = \bar{R}$ we have for $n = m$

$$R \cdot A_m = R \cdot U_m \tag{10}$$

and

$$\bar{R} \cdot B_m = \bar{R} \cdot V_m \tag{11}$$

The bridge inputs are interconnected such that $U_m = V_m$ as shown in Figure 4, and (10) becomes

$$R \cdot A_m = R \cdot V_m \tag{12}$$

The phase-sensitive bridge is driven from the magnetic sensor output windings such that for forward-direction torquing

$$V_{mp} = \sum_k T_{kp} \left[R C_{mk} P_k + \bar{R} D_{mk} Q_k \right], \quad \begin{matrix} m = 1, 2, 3 \\ k = 1 \text{ thru } 6 \end{matrix} \tag{13}$$

where

T_{kp} = elements of the stator-tooth excitation matrix. Equals logical 1 for k^{th} stator tooth active (opposite rotor pole piece) and logical 0 for k^{th} tooth inactive

C_{mk} = elements of the in-reference phase boolean connection matrix. Equals logical 1 for connection between k^{th} in-reference phase sensor winding and m^{th} bridge input, and logical 0 for no connection

D_{mk} = elements of the out-of-reference phase boolean connection matrix. Equals logical 1 for connection between k^{th} out-of-reference phase sensor winding and m^{th} bridge input, and logical 0 for no connection

P_k = elements of in-reference phase sensor output-winding vector. Equals logical 1 for in-reference phase output winding on k^{th} stator tooth and logical 0 for no winding

Q_k = elements of out-of-reference phase sensor output-winding vector. Equals logical 1 for out-of-reference phase output winding on k^{th} stator tooth and logical 0 for no winding

The sensor magnetic structure is such that the stator teeth are energized two at a time

$$k \equiv \ell, \ell + 1, \text{ mod } 6 \qquad \ell = 1 \text{ thru } 6$$

as the rotor assumes successive angular positions, $\theta = (p - 1)\pi/3$. Thus

$$\sum_k T_{kp} C_{mk} P_k = C_{m\ell} P_\ell + C_{m(\ell+1)} P_{\ell+1} \tag{14}$$

and

$$\sum_k T_{kp} D_{mk} Q_k = D_{m\ell} Q_\ell + D_{m(\ell+1)} Q_{\ell+1} \tag{15}$$

Substituting from (14) and (15) into (13), and combining with (11) and (12) yields

$$R \cdot A_m = R \cdot [C_{m\ell} P_\ell + C_{m(\ell+1)} P_{\ell+1}] \tag{16}$$

and

$$\bar{R} \cdot B_m = \bar{R} \cdot [D_{m\ell} Q_\ell + D_{m(\ell+1)} Q_{\ell+1}] \tag{17}$$

where it is recognized that $V_m = V_{mp}$ for all p. Conditions (2) and (3) for forward direction torquing are thus satisfied by the following system of boolean equations

$$C_{a\ell} P_\ell + C_{a(\ell+1)} P_{\ell+1} = 1 \tag{18}$$

$$D_{\beta\ell} Q_\ell + D_{\beta(\ell+1)} Q_{\ell+1} = 1 \tag{19}$$

$$C_{m\ell} P_\ell + C_{m(\ell+1)} P_{\ell+1} = 0, m \neq \alpha \tag{20}$$

$$D_{m\ell} Q_\ell + D_{m(\ell+1)} Q_{\ell+1} = 0, m \neq \beta \tag{21}$$

Index p depends on the relative angular positions of the rotor and stator in the torque motor magnetic structure, and index ℓ depends on the relative angular positions of the rotor and stator in the sensor magnetic structure. They are related by

$$\ell = \pm p + \zeta, \text{ mod } 6 \qquad \ell = 1 \text{ thru } 6 \tag{22}$$

where ζ is a constant dependent on the relative angular positions of both structures, and where the plus or minus sign is selected depending on the direction which the sensor is mounted on the shaft. Expansion of equations (18) through (21) subject to conditions (2), (3), and (22) yields the tabulated results of Figure 6. A simple solution to these equations utilizing a maximum number of logical zeros gives the stator tooth excitation matrix, and the boolean connection matrices and sensor winding vectors required for forward-direction torquing, Figure 7.

The armature switching sequence required for reverse-direction torquing of the torque motor is given by relations (4) and (5), and also in Figure 5. The reverse-direction logic can be obtained by reversing the time-phase of the bridge input signals or the bridge inhibit signals. The method used in the controller-commutator design reverses the time-phase of the bridge input signals by controlling the phase of the sensor drive signal. For reverse-direction operation equation (13) becomes

$p = 1,\ \ell = 1,\ \alpha = 1,\ \beta = 2$

$C_{11} P_1 + C_{12} P_2 = 1$

$D_{21} Q_1 + D_{22} Q_2 = 1$

$C_{21} P_1 = 0,\ C_{22} P_2 = 0,\ C_{31} P_1 = 0,\ C_{32} P_2 = 0$

$D_{11} Q_1 = 0,\ D_{12} Q_2 = 0,\ D_{31} Q_1 = 0,\ D_{32} Q_2 = 0$

$p = 2,\ \ell = 6,\ \alpha = 1,\ \beta = 3$

$C_{16} P_6 + C_{11} P_1 = 1$

$D_{36} Q_6 + D_{31} Q_1 = 1$

$C_{26} P_6 = 0,\ C_{21} P_1 = 0,\ C_{36} P_6 = 0,\ C_{31} P_1 = 0$

$D_{16} Q_6 = 0,\ D_{11} Q_1 = 0,\ D_{26} Q_6 = 0,\ D_{21} Q_1 = 0$

$p = 3,\ \ell = 5,\ \alpha = 2,\ \beta = 3$

$C_{25} P_5 + C_{26} P_6 = 1$

$D_{35} Q_5 + D_{36} Q_6 = 1$

$C_{15} P_5 = 0,\ C_{16} P_6 = 0,\ C_{35} P_5 = 0,\ C_{36} P_6 = 0$

$D_{15} Q_5 = 0,\ D_{16} Q_6 = 0,\ D_{25} Q_5 = 0,\ D_{26} Q_6 = 0$

$p = 4,\ \ell = 4,\ \alpha = 2,\ \beta = 1$

$C_{24} P_4 + C_{25} P_5 = 1$

$D_{14} Q_4 + D_{15} Q_5 = 1$

$C_{14} P_4 = 0,\ C_{15} P_5 = 0,\ C_{34} P_4 = 0,\ C_{35} P_5 = 0$

$D_{24} Q_4 = 0,\ D_{25} Q_5 = 0,\ D_{34} Q_4 = 0,\ D_{35} Q_5 = 0$

$p = 5,\ \ell = 3,\ \alpha = 3,\ \beta = 1$

$C_{33} P_3 + C_{34} P_4 = 1$

$D_{13} Q_3 + D_{14} Q_4 = 1$

$C_{13} P_3 = 0,\ C_{14} P_4 = 0,\ C_{23} P_3 = 0,\ C_{24} P_4 = 0$

$D_{23} Q_3 = 0,\ D_{24} Q_4 = 0,\ D_{33} Q_3 = 0,\ D_{34} Q_4 = 0$

$p = 6,\ \ell = 2,\ \alpha = 3,\ \beta = 2$

$C_{32} P_2 + C_{33} P_1 = 1$

$D_{22} Q_2 + D_{23} Q_3 = 1$

$C_{12} P_2 = 0,\ C_{13} P_3 = 0,\ C_{22} P_2 = 0,\ C_{23} P_3 = 0$

$D_{12} Q_2 = 0,\ D_{13} Q_3 = 0,\ D_{32} Q_2 = 0,\ D_{33} Q_3 = 0$

Figure 6–Phase-Controlled Logic Equations for Forward-Direction Torquing

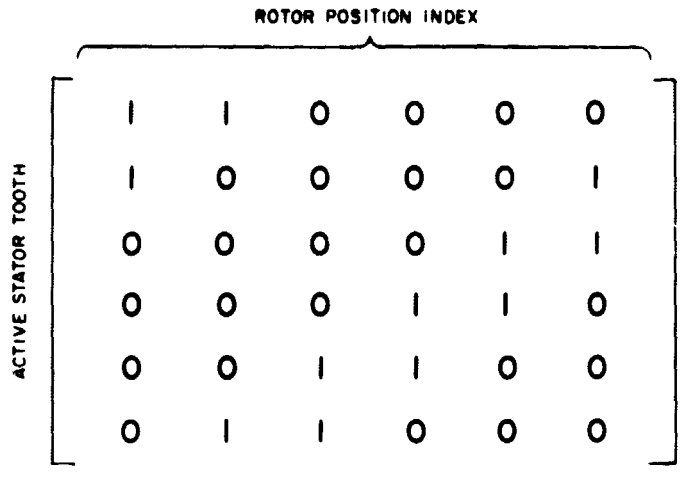

(a) STATOR TOOTH EXCITATION MATRIX FOR $\ell \equiv -p + 2$, MOD 6.

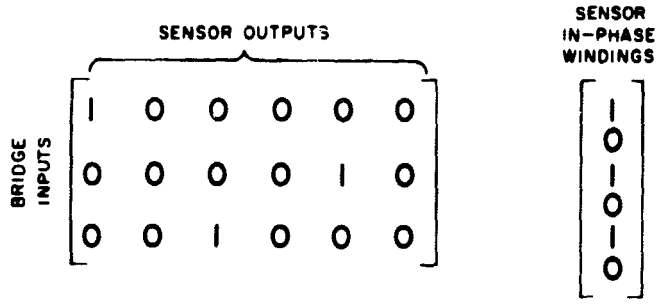

(b) IN-REFERENCE PHASE CONNECTION MATRIX AND SENSOR WINDING VECTOR FOR $\ell \equiv -p + 2$, MOD 6.

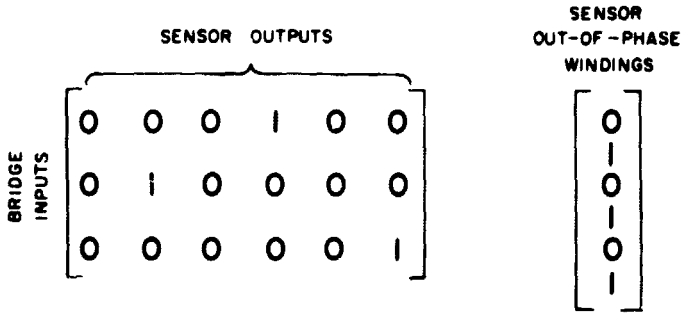

(c) OUT-OF-REFERENCE PHASE CONNECTION MATRIX AND SENSOR WINDING VECTOR FOR $\ell \equiv -p + 2$, MOD 6.

Figure 7–Boolean Excitation and Connection Matrices and Winding Vectors for Magnetic Sensor and Phase-Sensitive Bridge

$$V_{mp} = \sum_{k} T_{kp} \left[\bar{R}\, C_{mk}\, P_k + R\, D_{mk}\, Q_k \right], \quad \begin{matrix} m = 1,\ 2,\ 3 \\ k = 1 \text{ thru } 6 \end{matrix} \tag{23}$$

and this leads to the following system of boolean equations

$$C_{\delta \ell}\, P_{\ell} + C_{\delta(\ell+1)}\, P_{\ell+1} = 1 \tag{24}$$

$$D_{\gamma \ell}\, Q_{\ell} + D_{\gamma(\ell+1)}\, Q_{\ell+1} = 1 \tag{25}$$

$$C_{m \ell}\, P_{\ell} + C_{m(\ell+1)}\, P_{\ell+1} = 0, \quad m \neq \delta \tag{26}$$

$$D_{m \ell}\, Q_{\ell} + D_{m(\ell+1)}\, Q_{\ell+1} = 0, \quad m \neq \gamma \tag{27}$$

in a manner similar to that giving equations (18) through (21). Comparison of relations (2) through (4) shows that for any given value of index p

$$\alpha = \delta \tag{28}$$

$$\beta = \gamma \tag{29}$$

Substituting (28) and (29) into equations (24) through (27) and comparing with (18) through (21) shows that the reverse-direction boolean equations are the same as the forward-direction equations. The boolean matrices and vectors of Figure 7 thus provide the logic required for both forward and reverse operation of the torque motor.

This result is important in achieving circuit simplicity in that no additional logic circuitry is needed to obtain a bidirectional drive capability. This fact combined with the simplicity of the sensor winding and connection configurations, and the need for only a single magnetic sensor contribute substantially to reducing complexity of the controller-commutator design.

IV. MAGNETIC ROTOR-POSITION-AND-RATE SENSOR

The purpose of this section of the report is to present a magnetic sensor design that provides (1) rotor-position sensing for brushless DC commutation, (2) angular-rate information for controlled-damping and rate-limiting of the solar array at orbital rates, and (3) time-phase dependent outputs for implementation of bidirectional torquing logic developed in Section III. These functions are simply and effectively combined into a single sensor so that the complexity of an individually mechanized design is avoided.

The basic configuration of the magnetic sensor is shown in Figure 8. The sensor structure consists of a stator and rotor portion, each made of readily polarized magnetic material. The stator construction is unsymmetrical with teeth that are offset from positions that are diametrically opposite each other. Windings N are the sensor primary or excitation windings, and winding N_5 is

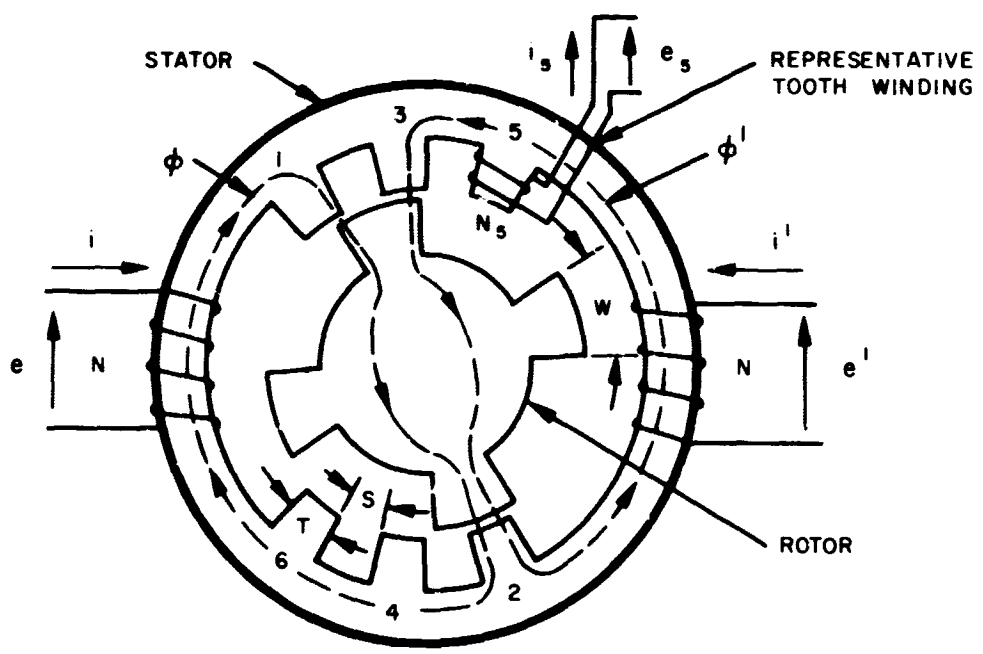

Figure 8–Basic Configuration of Offset-Tooth Magnetic Rotor-Position-and-Rate Sensor

representative of the sensor output or pick-off windings on each tooth of the stator structure. The sensor is operated by exciting input windings N in opposition to each other so that the flux is driven through the stator teeth. Flux flows through the teeth that are lined up with the rotor poles and output signals are generated only in the windings on those teeth.

The sensor performance parameters of interest are (1) gain, (2) bandwidth, (3) interactions between outputs, and (4) input drive requirements. These quantities are optimized by appropriately selecting the geometric proportions of the sensor magnetic structure and sensor loading conditions. The options that are available to the designer depend on whether the sensor is to be used exclusively for commutation or whether both the commutation and rate-sensing functions are to be integrated into the same device.

Simplified expressions for the sensor performance parameters are derived in Appendix I for magnetic structure geometries that are constrained by the relation

$$S < W < S + 2T \tag{1}$$

The derived quantities apply under conditions of equal resistive loading, R, on each sensor output, and are given by

$$\bar{G}_{n10} = \frac{A_1}{A_1 + A_3} \tag{2}$$

$$\bar{G}_{n1\infty} = \frac{R_1}{R_1 + R_3} = \frac{1}{2} \tag{3}$$

$$BW_{nm} = \frac{A_2}{A_3}\bigg|_{A_1 \to 0} \tag{4}$$

$$\bar{Z}_{nm} = \frac{2}{1 + BW_{nm} + 2j\,\omega_n} \tag{5}$$

where (2) is the normalized low-frequency gain for output 1, (3) is the normalized high-frequency gain for output 1, (4) is the minimum normalized bandwidth of the sensor, and (5) is the normalized input impedance of the sensor corresponding to minimum normalized bandwidth. The symbols in the above equations are defined in Appendix I.

It is seen from equation (2) that the sensor low-frequency gain is dependent on the geometry of the magnetic structure and the rotor angular position, since A_1, A_3 are so dependent, but is independent of the sensor loading conditions. Thus, the sensor can be designed for indefinitely large drive capability by operating at sufficiently low frequency. The magnetic structure and winding turns must be sufficiently large however to avoid saturating the sensor magnetic material.

Equation (3) shows that the high-frequency gain depends on the sensor loading conditions but is independent of the magnetic structure geometry (at least within the constraints of relation (1)) and the rotor angular position. The high frequency gain is thus constant and for equal resistive loading on each sensor output is equal to 1/2 of the maximum low-frequency gain.

The minimum normalized bandwidth given in equation (4) is seen also to depend on the magnetic structure geometry and rotor angular position of the sensor. For a magnetic structure in which $W \to S$, $A_3 \to 0$ and $BW_{nm} \to \infty$ so that a major advantage of the GSFC offset-tooth configuration is demonstrated. Namely, the offset-tooth sensor frequency response can be made indefinitely large for all angular positions of the rotor, and for arbitrarily large resistive loading, by selecting W sufficiently close to S. The maximum value of minimum normalized bandwith that can be achieved in this manner is eventually limited, however, by practical considerations of sensor leakage fluxes and winding resonances.

As $W \to S$ the low-frequency gain of the sensor approaches the characteristics of Figure 9, in which a theoretically infinite rate of transition is made from the sensor minimum output to maximum output levels. The actual rate of transition is limited, however, by flux fringing and maximum saturation flux density of the sensor magnetic material.

Increased normalized bandwidth of the sensor and rate of transition in the gain characteristic as $W \to S$ is obtained at the expense of increased input drive requirements. As seen in equation (5), the sensor input impedance at minimum output approaches zero for a sensor design in which the minimum normalized bandwidth is made indefinitely large. Thus the magnetic structure geometry $W \to S$ yields a nearly optimum sensor gain and bandwidth characteristic for commutation but puts a severe demand on the sensor driving source.

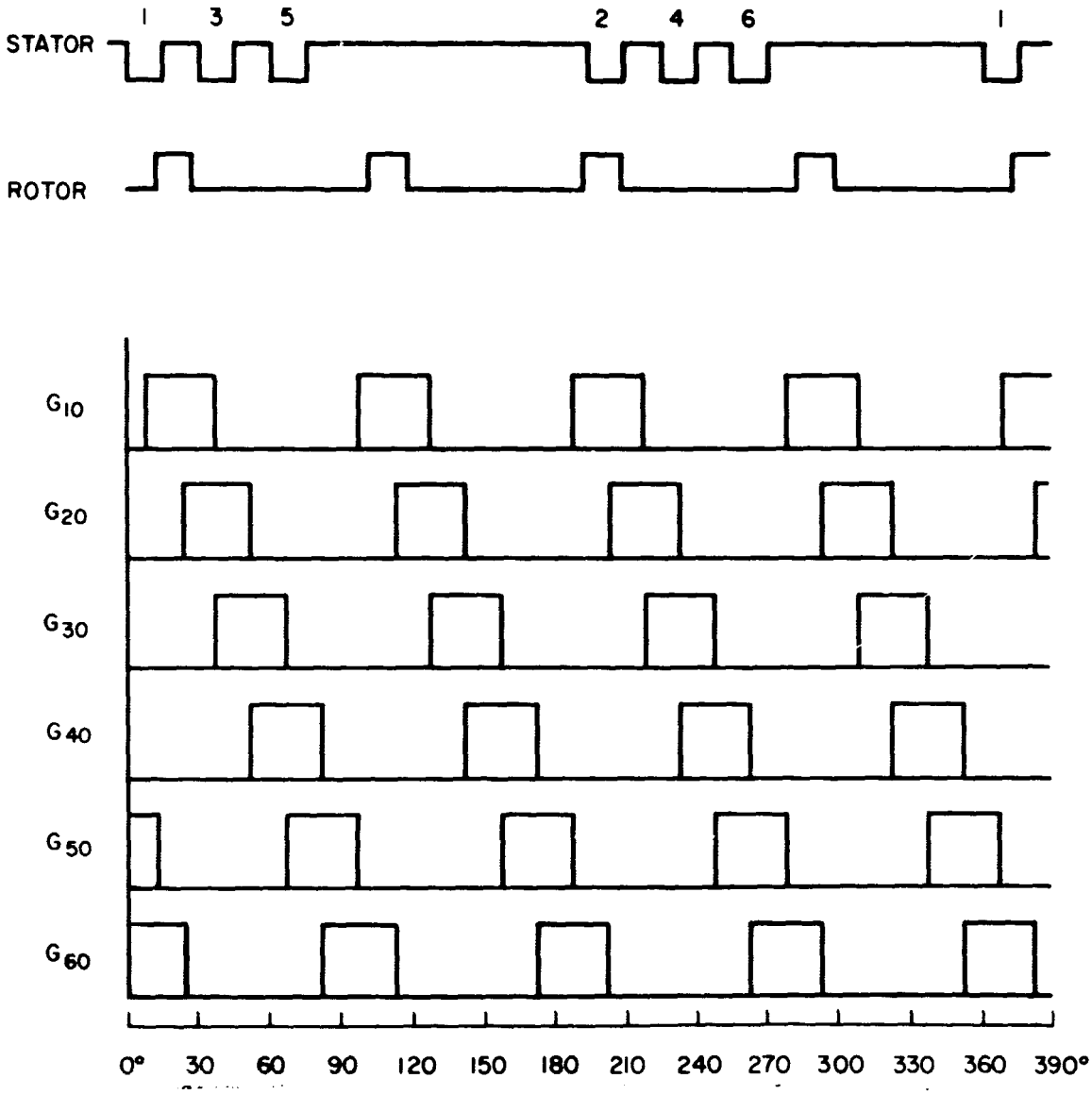

Figure 9–Low-Frequency Gain Characteristic of Magnetic Sensor for W = S

The magnetic structure of the offset-tooth sensor is readily proportional such that the transition interval from minimum to maximum low-frequency gain is linearly related to the rotor angular position. The offset-tooth design is thus inherently capable of simultaneously integrating rotor position information for commutation purposes and rate information for control purposes into the same magnetic structure. Such integration of the rate-sensing and commutation functions constrains the sensor geometry so that the choice W → S is no longer available to the designer.

The sensor low-frequency gain characteristic is piecewise linear for all angular positions of the rotor and the linear transition interval is maximum for a sensor geometry in which

$$W = S + T \tag{6}$$

For these sensor proportions, equations (2) through (5) for the normalized performance parameters become

$$\bar{G}_{n10} = \frac{A_1}{A_2} \tag{7}$$

$$\bar{G}_{n1\infty} = \frac{1}{2} \tag{8}$$

$$BW_{nm} = 1 \tag{9}$$

$$\bar{Z}_{nm} = \frac{1}{1 + j\omega_n} \tag{10}$$

The sensor low-frequency gain at output 1 is then

$$\bar{G}_{10} = -\frac{2N_1 A_1}{NA_2} \tag{11}$$

where maximum gain occurs at $A_1 = A_2$, giving

$$\bar{G}_{0\ max} = -\frac{2N_1}{N} \tag{12}$$

The sensor bandwidth and input impedance at minimum output are

$$BW_m = \omega_m = \frac{gR}{\mu_0 N_1^2 A_2} \tag{13}$$

and

$$\bar{Z}_m = \frac{R}{8}\left(\frac{N}{N_1}\right)^2 \frac{j\omega}{\frac{gR}{\mu_0 N_1^2 A_2} + j\omega} \tag{14}$$

so that the bandwidth increases indefinitely, within practical limits, and the impedance remains finite for R arbitrarily large. Thus, these desired performance characteristics are obtained at the expense of limited sensor loading.

Linearity of the sensor transition interval is not sufficient in itself to provide a rate-sensing capability suitable for use in direct-drive solar array control applications. It is further required that rate information be available for all angular positions of the rotor so that a linear transition interval of at least one sensor output must occur at all rotor positions. This continuous, 360° coverage of rate information is achieved in the offset-tooth design with a stator tooth width

$$S = T \tag{15}$$

as shown in the configuration of Figure 8. Overlapping of the linear transition regions results for $S < T$. The low-frequency gain of the sensor as a function of rotor angular position for the integrated sensor magnetic structure geometry, $W = S + T$ and $S = T$, is shown in Figure 10.

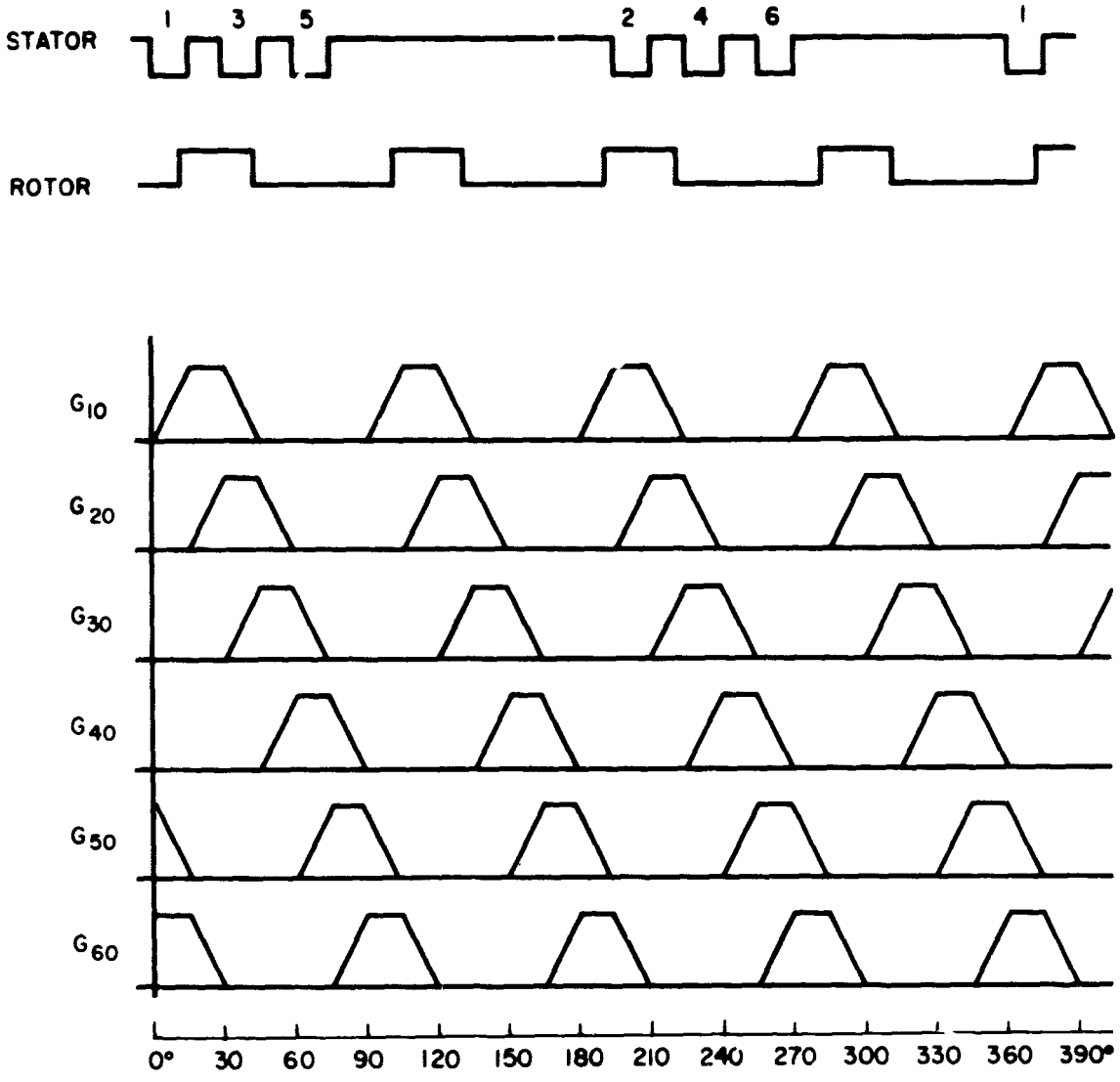

Figure 10–Low-Frequency Gain Characteristic of Magnetic Sensor for W = S + T and S = T

Direction-of-rotation information is obtained from the sensor by combining the sensor outputs in a logical arrangement such that the rate signal is derived from:

1. only the positive slopes or the negative slopes of the low-frequency gain characteristic for both directions of rotation. The rate signal is then obtained from a single channel, with one polarity signal for CW rotation and opposite polarity for CCW rotation.

or

2. only the positive slopes for one direction of rotation and only the negative slopes for the other direction. The rate signal is then of the same polarity for both directions of rotation but occurs in two separate channels, one for CW rotation and the other for CCW rotation.

The angular resolution capability of the sensor is such that both rate magnitude and direction information is available within angular increments of a fraction of a degree.

The low-frequency gain of outputs 1 and 3 are given by

$$\bar{G}_{10} = -\frac{2N_1}{N}\,\frac{A_1}{A_1 + A_3} \tag{16}$$

and

$$\bar{G}_{30} = -\frac{2N_1}{N}\,\frac{A_3}{A_1 + A_3} \tag{17}$$

Since commutation occurs when $G_{10} = G_{30}$ we get from (12), (16) and (17) that $A_1 = A_3$, and

$$\bar{G}_{10} = \frac{1}{2}\,\bar{G}_{0\ max} \tag{18}$$

at the commutation points. Thus equation (18) shows that commutation occurs at a threshold voltage level equal to one-half of the maximum sensor output, at least for magnetic structure geometries within the constraints of relation (1).

V. TORQUE/SPEED CONTROL

The torque/speed control functions of the solar array drive system are also functionally-integrated into the torque motor commutation circuitry. These

control functions are introduced into the bridge portion of the commutator (after the magnetic sensor) to avoid interactions with the magnetic sensor rotor position and rate signals. This section of the report discusses the bridge circuit operation and describes how integration of the torque/speed control function is achieved.

The circuit of Figure 11 is the basic building block of the commutator bridge. It consists of transistor, Q, and nonlinear magnetic core, T, connected in a blocking oscillator configuration[4]. The circuit is designed with a loop-gain slightly greater than unity so that it operates essentially as a "magnetic core

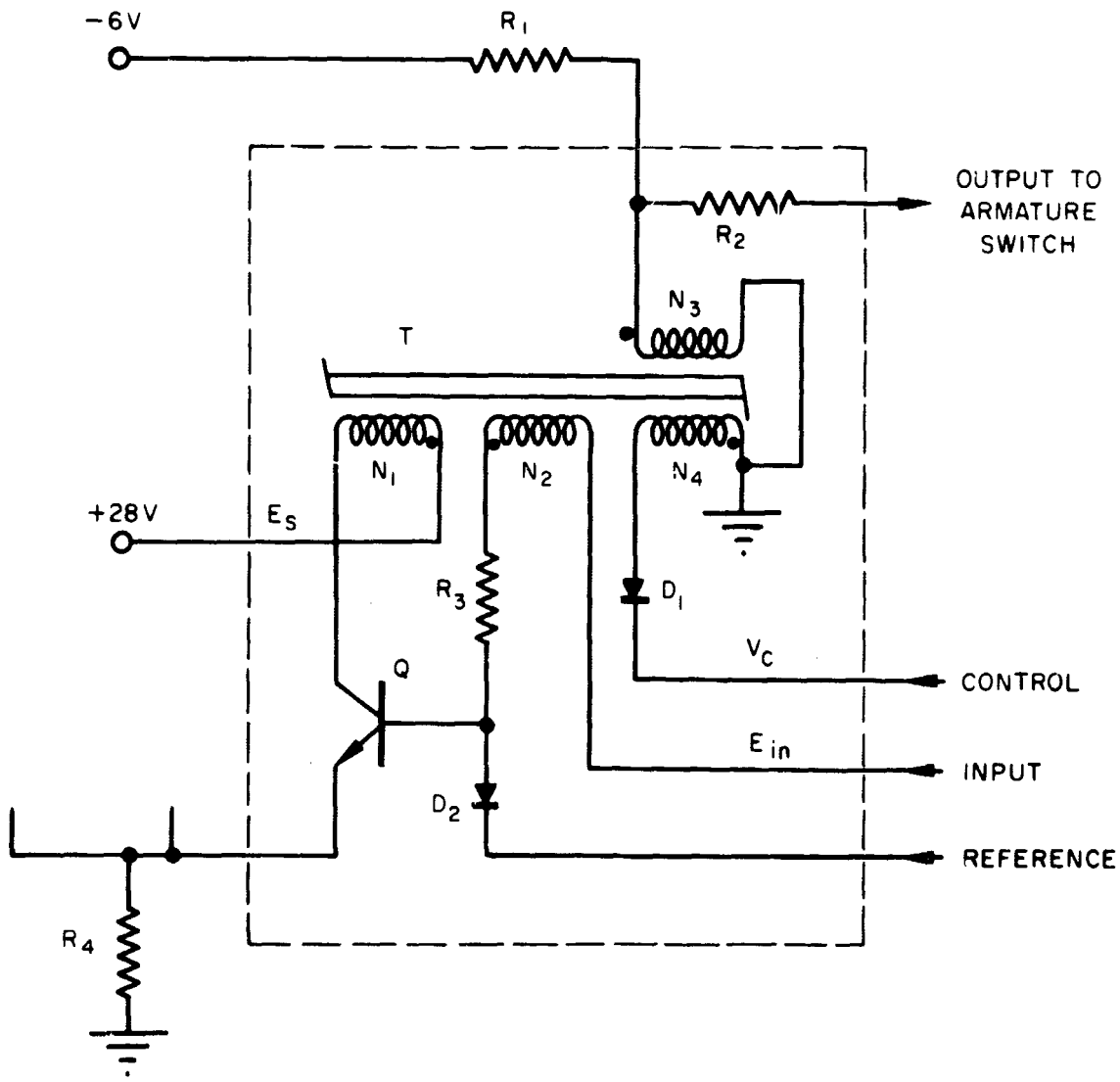

Figure 11–Basic Magnetic Core Schmitt Circuit

Schmitt" circuit (MCS). Two important performance characteristics result from such a design.

1. Turn-on and turn-off of the armature switches is regenerative so that damage due to excessive heat dissipation in the switches at or near the commutation points is avoided. This feature is required for operation at stall or at the very low angular rates (approximately 0.01 rpm or less) occurring in direct-drive solar array control applications.

and

2. Hysteresis is made small so that regenerative drive of the output is effectively controlled by the AC input signal thus rendering the circuit insensitive to extraneous disturbances. The minimum permissible hysteresis is governed by the maximum decay in the triggering waveform. Insufficient hysteresis causes premature termination of the MCS pulse interval when the decayed input waveform falls below the switching threshold level.

Current amplification is provided by both the transistor and magnetic core. The output from the core is taken from winding N_3 which also serves to reset the core during the blocking period. Operation of the circuit is inhibited through diode D_2 except for input signals that are in-phase with the reference signal. Common emitter resistors in the upper-leg and lower-leg sections of the bridge permit only one armature switch in each section to be actuated at any given time.

The MCS circuit drives the armature switches during only one half of each cycle of operation. Continuous conduction of the upper-leg switches is obtained by filtering the MCS output, using a full-wave version of the MCS circuit, or by employing armature switching transistors with long minority carrier storage time (50 to 100 μsec) to sustain conduction between successive half-cycle driving periods.

Torque/speed control functions are readily integrated into the commutator circuitry by controlling the reset level of core flux in the lower-leg MCS circuits of the bridge. This is done by applying an external control voltage, V_c, across winding N_4 through diode D_1. V_c limits the rate of flux reversal during the reset interval and D_1 decouples the control voltage from the core during the driving interval. Variation of the core flux reset level produces a corresponding variation of the armature switch conduction time so that pulse-width modulation of the armature excitation is obtained. The armature switch conduction time, T_f, is given in terms of the core reset time, T_r, by the relation

$$\left[\frac{N_1}{R_4} E_s + \left(\frac{N_1 + N_2}{R_3}\right)(E_s - E_{in})\right] T_1 = \left[\frac{(N_1 + N_2)^2}{R_3} + \frac{N_3^2}{R_2} + \frac{N_1^2}{R_4}\right]\frac{V_c T_r}{N_4} \quad (1)$$

where the circuit parameters and voltages are given in Figure 11. The core resets for one-half period of oscillation giving

$$T_r = \frac{T}{2} \quad (2)$$

for all angular positions of the rotor except at or near the commutation points, where the collector winding mmf, $N_1 i_1$, may not be sufficient to override the reset mmf, $N_3 i_3$, during the time interval $T_1 < t < T/2$. In this case the core resets throughout the entire blocking period so that the reset time becomes

$$T_r = T - T_1 \quad (3)$$

Combining equation (2) with (1) gives the armature switching duty ratio, T_1/T, as a linear function of the external control voltage, V_c, as follows

$$\left[\frac{N_1}{R_4} E_s + \left(\frac{N_1 + N_2}{R_3}\right)(E_s - E_{in})\right]\left(\frac{T_1}{T}\right) = \left[\frac{(N_1 + N_2)^2}{R_3} + \frac{N_3^2}{R_2} + \frac{N_1^2}{R_4}\right]\frac{V_c}{2N_4} \quad (4)$$

Under conditions where equation (3) applies the armature switch duty ratio is nonlinearly related to the control voltage. The maximum theoretical departure from the linear characteristic is approximately 17% of the full-scale duty ratio and occurs at approximately 41% of the full-scale value of control voltage. In applications where this nonlinearity is objectionable it can be removed by gating the core reset voltage with a single transistor driven out-of-phase with the reference signal φ.

Since the torque motor operates under armature-controlled conditions with pulsed excitation voltage the following basic equations apply.

$$\ell = K_L\, i \tag{5}$$

$$e_s = K_L\, \dot{\theta} \tag{6}$$

$$e_m = R_a\, i + L_a \frac{di}{dt} + e_s \tag{7}$$

where

ℓ = electromagnetic developed torque

i = armature current

$\dot{\theta}$ = shaft speed

e_s = speed voltage

e_m = motor excitation voltage

K_L = motor torque-sensitivity

R_a = armature resistance

L_a = armature inductance

Substituting from (5) and (6) into (7) and taking the time average of the resulting equation over one period of the excitation voltage under essentially steady state conditions, we obtain

$$E_s \left(\frac{T_1}{T}\right) = \frac{R_a}{K_L} L + K_L\, \dot{\theta} \tag{8}$$

where

L = average motor torque

$\dot{\theta}$ = average shaft speed

Equation (8) gives the motor torque-speed characteristic when operating under pulsed conditions. Since the armature winding time constant is long compared to the excitation period of 100μ sec the armature current is filtered and essentially steady motor torque is produced. The left member of (8) shows that the torque motor excitation level is modulated by controlling the armature switching duty-ratio.

By eliminating T_1/T between equations (4) and (8) L, Θ, and V_c are essentially linearly related as

$$\left[\frac{N_1}{R_4} + \left(\frac{N_1 + N_2}{R_3}\right)\left(1 - \frac{E_{in}}{E_s}\right)\right]\left(\frac{R_a}{K_L} L + K_L \dot{\Theta}\right) = \left[\frac{(N_1 + N_2)^2}{R_3} + \frac{N_3^2}{R_2} + \frac{N_1^2}{R_4}\right]\frac{V_c}{2N_4} \quad (9)$$

giving a torque/speed characteristic similar to a conventional permanent magnet DC torque motor. Thus torque/speed control is integrated into the commutation circuitry by duty-ratio modulating the level of torque motor excitation with external control voltage, V_c.

Pulse-modulation of the motor torque, L, can be achieved by applying gating signals at terminals a, b, or c that are of long duration compared to the torque motor armature winding time constant.

VI. RESULTS AND CONCLUSIONS

A laboratory model controller-commutator circuit, Figure 12, was built and tested, and important points of the design presented in this report were verified. The following test results were obtained: (1) Bidirectional drive of the torque motor using a single magnetic sensor and phase-controlled logic, (2) Torque/speed control using excitation-level modulation integrated into the commutator, (3) Normalized no-load speed versus control voltage characteristic, Figure 13, (4) Normalized stall torque versus control voltage characteristic, Figure 14, (5) MCS pulse-width versus control voltage characteristic both in the vicinity of and removed from the commutation point, Figure 15.

Waveform measurements made on the offset-tooth magnetic sensor show improved response, Figure 16a, and reduced interaction between outputs of the sensor, Figure 16b, as compared to earlier symmetrical designs.[1] Preliminary testing of the rate-sensing capabilities of the offset-tooth magnetic sensor, conducted at 0.1 rpm, shows that useable signal levels are obtainable at rotational speeds as low as orbital rate.

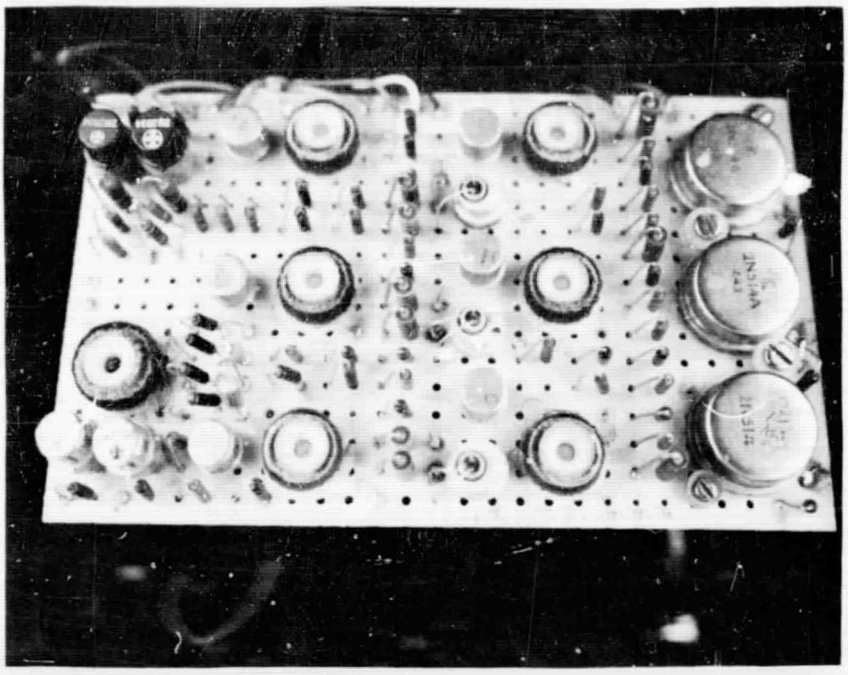

Figure 12--Laboratory Model of Functionally-Integrated Controller-Commutator

The combined analytical and experimental results presented in this report demonstrate the workability of the functionally-integrated concept in brushless, direct-drive solar array reorientation system design. The principles of phase-controlled logic, and integrated torque/speed control and rate-sensing have been applied in a controller-commutator in which the upper-leg armature switches are driven by MCS circuits with filtered outputs. This controller-commutator is being employed in a solar array reorientation system design that is brushless and without gearing throughout.

As suggested in Section III bidirectional drive of the torque motor can be achieved by phase-control of the bridge inhibit signals instead of the sensor output signals. The torque motor reversing function as well as torque/speed control is then achieved in the bridge portion of the controller-commutator circuitry. Such an arrangement essentially isolates the sensor rate signals from the other control function signals yielding a more nearly optimum design for applications in which rate control requirements are stringent.

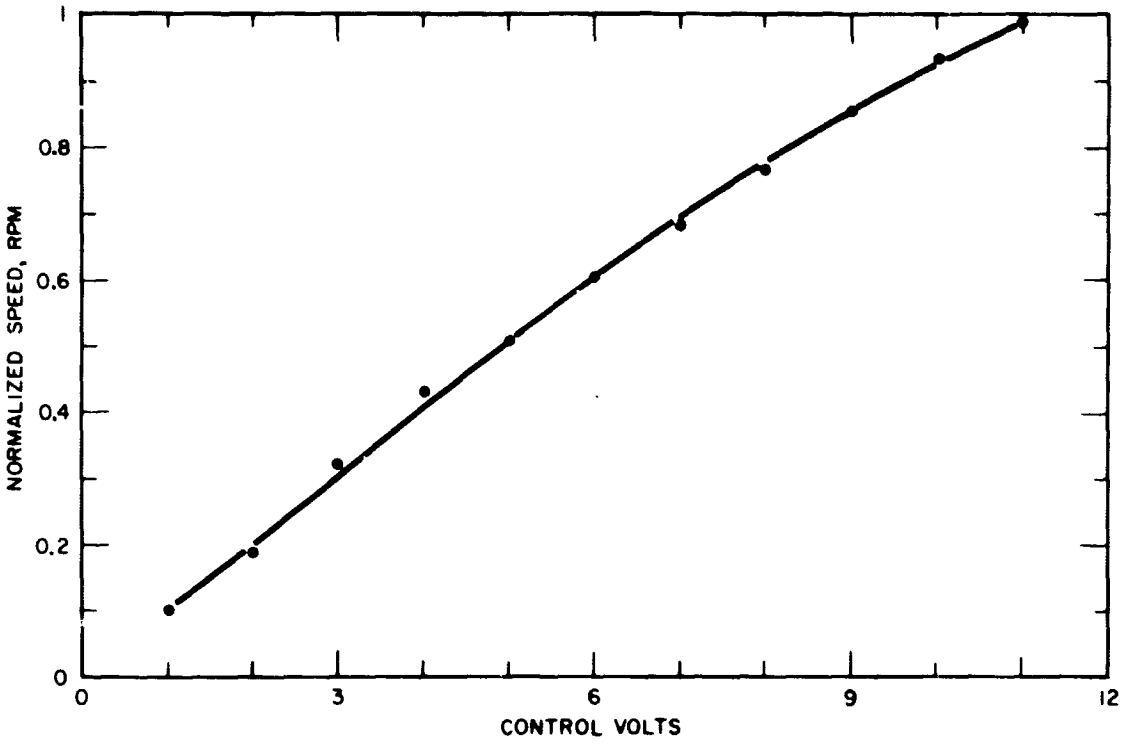

Figure 13–Normalized No-Load Speed vs Control Voltage

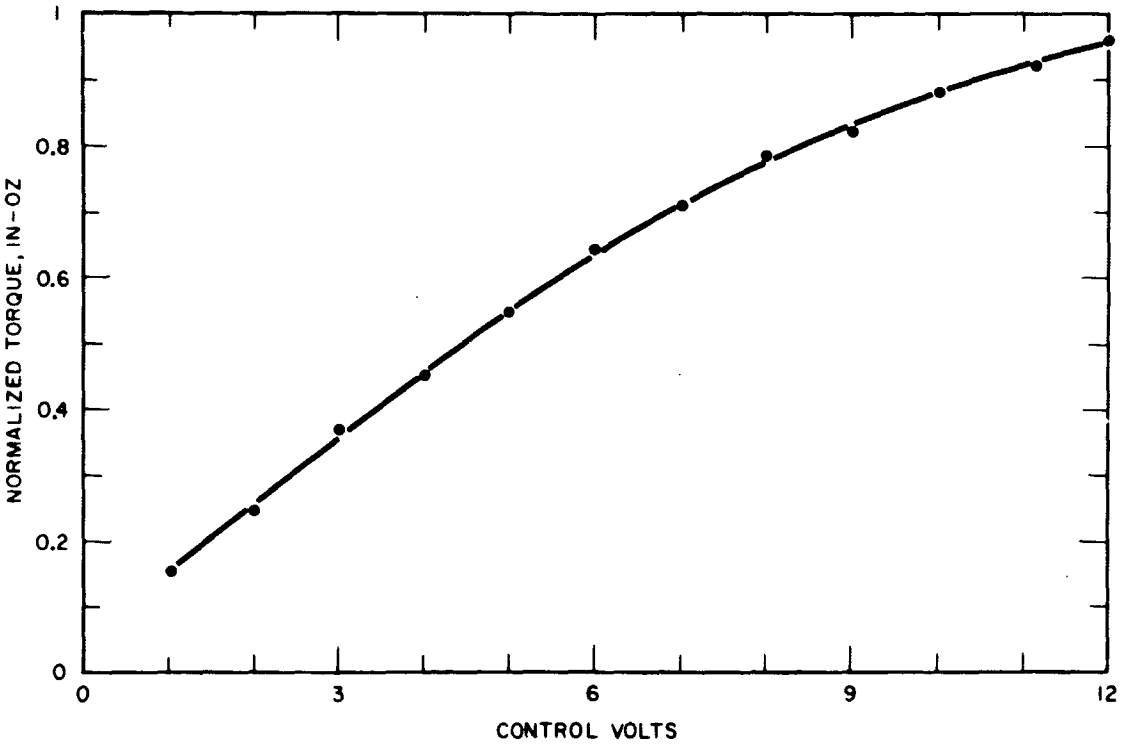

Figure 14–Normalized Stall Torque vs Control Voltage

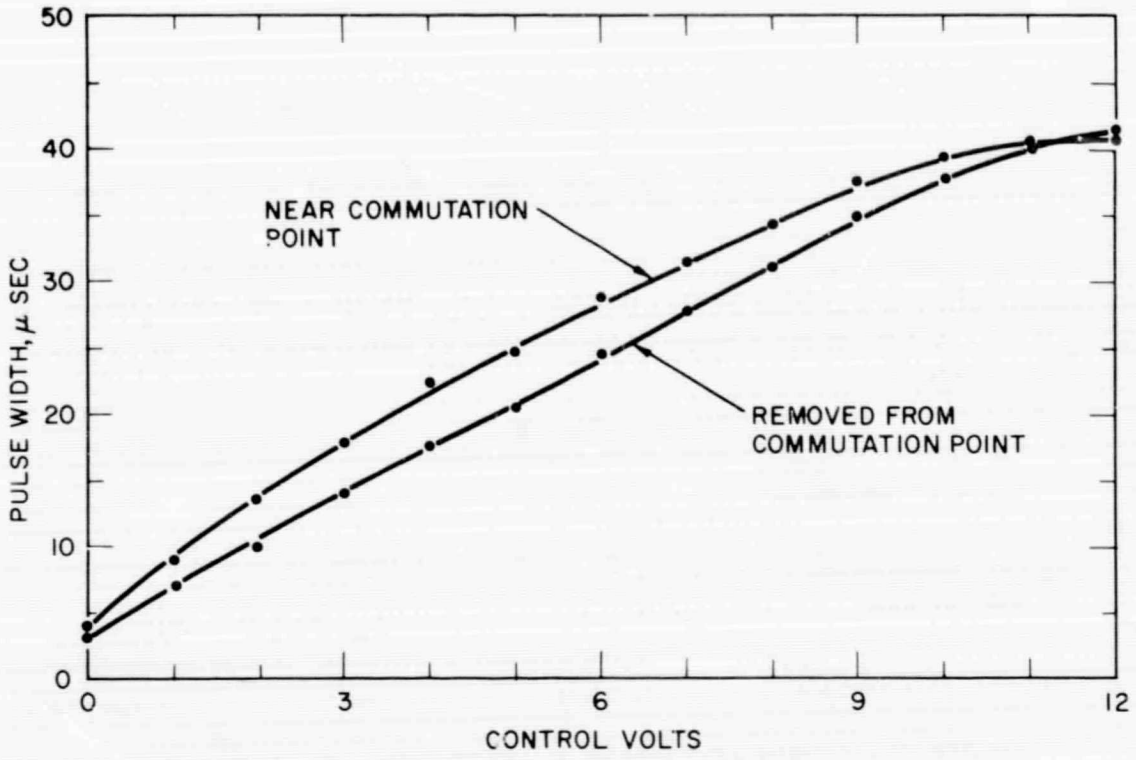

Figure 15–MCS Pulse-Width vs Control Voltage

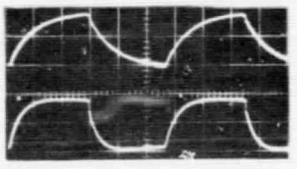

(a) RESPONSE WAVEFORMS WITH BALANCED LOADS OF 100 OHMS

Figure 16–Waveforms Showing Sensor Response and Interaction Between Outputs

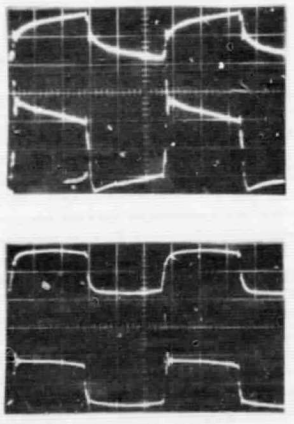

(b) INTERACTION WAVEFORMS WITH UNBALANCED LOADS OF 500 AND 2K OHMS

APPENDIX I

DERIVATION OF MAGNETIC SENSOR PERFORMANCE CHARACTERISTICS

The purpose of this appendix is to determine the dominant performance characteristics of the offset-tooth magnetic rotor-position-and-rate sensor. A simplified analysis of the sensor is undertaken in which the following assumptions are made,

1. the sensor magnetic circuit is unsaturated at all times throughout the cycle of operation

2. the magnetizing mmf within the magnetic material is small compared to the air-gap

3. flux leakage and fringing are negligible. (Leakage effects increase as the sensor length is decreased, the air-gap is increased, and the radial lengths of the rotor pole pieces and stator teeth are reduced.)

4. the frequency of operation is below that at which sensor winding capacitances and resonances become significant

The range of variation in magnetic structure geometry considered in the analysis is given by the relation

$$S < W < S + 2T \tag{1}$$

where S, W, and T are given in Figure 8. These limits are imposed because the magnetic circuit reluctance becomes very large at various angular positions of the rotor for a sensor design in which $W < S$, and the rise and fall or transition portions of the sensor output amplitudes become substantially nonlinear for $W > S + 2T$.

The sensor performance characteristics are dependent on the magnetic structure configuration and material, and winding arrangement and loading conditions. The sensor operation is described by field conditions within the sensor structure so that the analysis begins with the integral form of Maxwells equations specialized for quasi-stationary conditions[5]

$$\oint_S \bar{B} \cdot d\bar{a} = 0 \tag{2}$$

$$\oint_C \bar{H} \cdot d\bar{\ell} = I_c \tag{3}$$

$$\oint_C \bar{E} \cdot d\bar{\ell} = -\frac{d}{dt} \int_S \bar{B} \cdot d\bar{a} \tag{4}$$

Applying these relations to the configuration of Figure 8 and combining and simplifying the equations obtained, we get

$$e_1 + \frac{\mu_0 N_1 A_1 A_3}{g(A_1 + A_3)} \frac{d}{dt}(N_1 i_1 - N_3 i_3) = -\frac{2N_1 A_1 e}{N(A_1 + A_3)} \tag{5}$$

$$e_2 = -\frac{2N_2}{N} e \tag{6}$$

$$e_3 + \frac{\mu_0 N_3 A_1 A_3}{g(A_1 + A_3)} \frac{d}{dt}(N_3 i_3 - N_1 i_1) = -\frac{2N_3 A_3 e}{N(A_1 + A_3)} \tag{7}$$

$$\frac{e_1}{N_1 A_1} + \frac{e_2}{N_2 A_2} = -\frac{\mu_0}{g} \frac{d}{dt}(N_1 i_1 + N_2 i_2 + N i) \tag{8}$$

where

N = primary winding turns on each stator section

N_1, N_2, N_3 = winding turns on stator teeth 1, 2, 3 respectively

A_1, A_2, A_3 = active area of stator teeth 1, 2, 3 respectively (area opposite rotor pole piece). For the conditions of this analysis $A_1 = A_1(\theta)$ and $A_3 = A_3(\theta)$ are functions of the rotor angular position, θ, while A_2 is constant and is equal to the total stator tooth area

g = sensor air-gap length

e = primary excitation voltage

i = primary excitation current in each stator winding

e_1, e_2, e_3 = sensor output voltages from windings N_1, N_2, N_3 respectively

i_1, i_2, i_3 = sensor output currents from windings N_1, N_2, N_3 respectively

For a sensor winding design $N_1 = N_2 = N_3$ and output loading such that $e_1 = R_1 i_1$, $e_2 = R_2 i_2$, and $e_3 = R_3 i_3$, equations (5) thru (8) can be combined to give

$$e_1 + \frac{\mu_0 N_1^2 A_1 A_3}{g(A_1 + A_3)} \left(\frac{1}{R_1} + \frac{1}{R_3}\right) \frac{de_1}{dt} = -\frac{2N_1 A_1}{N(A_1 + A_3)} \left(e + \frac{\mu_0 N_1^2 A_3}{g R_3} \frac{de}{dt}\right) \tag{9}$$

$$e_2 = -\frac{2N_1}{N} e \tag{10}$$

$$e_3 + \frac{\mu_0 N_1^2 A_1 A_3}{g(A_1 + A_3)} \left(\frac{1}{R_3} + \frac{1}{R_1}\right) \frac{de_3}{dt} = -\frac{2N_1 A_3}{N(A_1 + A_3)} \left(e + \frac{\mu_0 N_1^2 A_1}{g R_1} \frac{de}{dt}\right) \tag{11}$$

$$\frac{g}{\mu_0 N_1^2} \left[\frac{A_1 + A_2 + A_3}{A_2(A_1 + A_3)}\right] e +$$

$$+ \frac{1}{R_1 + R_3} \left[\frac{R_1 + R_2 + R_3}{R_2} + \frac{A_1 A_3}{A_2(A_1 + A_3)} \left(2 + \frac{R_1(A_1 + A_2)}{R_3 A_1} + \frac{R_3(A_2 + A_3)}{R_1 A_3}\right)\right] \frac{de}{dt} +$$

$$+ \left(\frac{R_1 + R_2 + R_3}{R_1 R_2 R_3}\right) \frac{\mu_0 N_1^2 A_1 A_3}{g(A_1 + A_3)} \frac{d^2 e}{dt^2} = \frac{1}{2} \left(\frac{N}{N_1}\right)^2 \left[\frac{di}{dt} + \frac{\mu_0 N_1^2 A_1 A_3 (R_1 + R_3)}{g(A_1 + A_3) R_1 R_3} \frac{d^2 i}{dt^2}\right] \tag{12}$$

The sensor primary windings are taken in parallel opposition giving

$$e_{in} = e \tag{13}$$

$$i_{in} = 2\,i \tag{14}$$

Substituting (13) and (14) into equations (9) through (12) and transforming the resulting system of equations to the frequency domain we have

$$\left[1 + j\omega\left(\frac{1}{R_1} + \frac{1}{R_3}\right)\frac{\mu_0 N_1^2 A_1 A_3}{g\,(A_1 + A_3)}\right]\bar{E}_1 = -\frac{2N_1 A_1}{N(A_1 + A_3)}\left(1 + j\omega\frac{\mu_0 N_1^2 A_3}{g R_3}\right)\bar{E}_{in} \tag{15}$$

$$\bar{E}_2 = -\frac{2N_1}{N}\bar{E}_{in} \tag{16}$$

$$\left[1 + j\omega\left(\frac{1}{R_1} + \frac{1}{R_3}\right)\frac{\mu_0 N_1^2 A_1 A_3}{g\,(A_1 + A_3)}\right]\bar{E}_3 = -\frac{2N_1 A_3}{N(A_1 + A_3)}\left(1 + j\omega\frac{\mu_0 N_1^2 A_1}{g R_1}\right)\bar{E}_{in} \tag{17}$$

$$\left[\frac{g\,(A_1 + A_2 + A_3)}{\mu_0 N_1^2 A_2\,(A_1 + A_3)} - \omega^2\left(\frac{R_1 + R_2 + R_3}{R_2}\right)\frac{\mu_0 N_1^2 A_1 A_3}{g\,(A_1 + A_3)} + \right.$$

$$\left. + \frac{j\omega}{R_1 + R_3}\left(\frac{R_1 + R_2 + R_3}{R_2} + \frac{A_1 A_3}{A_2\,(A_1 + A_3)}\left(2 + \frac{R_1\,(A_1 + A_2)}{R_3 A_1} + \frac{R_3\,(A_2 + A_3)}{R_1 A_3}\right)\right)\right]\bar{E}_{in} =$$

$$= \frac{\omega}{4}\left(\frac{N}{N_1}\right)^2\left(j - \frac{\omega\mu_0 N_1^2 A_1 A_3\,(R_1 + R_3)}{g\,(A_1 + A_3)\;R_1 R_3}\right)\bar{I}_{in} \tag{18}$$

The sensor gain, $\bar{G}$, is defined as the ratio of output voltage to input voltage at frequency ω. Thus from equations (15) through (17) we have

$$\bar{G}_1 = \frac{\bar{E}_1}{\bar{E}_{in}} = \frac{1 + j\omega a_1}{1 + j\omega b}\,\bar{G}_{10} \tag{19}$$

$$\bar{G}_2 = \frac{\bar{E}_2}{\bar{E}_{in}} = \bar{G}_{20} \tag{20}$$

$$\bar{G}_3 = \frac{\bar{E}_3}{\bar{E}_{in}} = \frac{1 + j\omega a_3}{1 + j\omega b}\,\bar{G}_{30} \tag{21}$$

where

$$a_1 = \frac{\mu_0 N_1^2 A_3}{g R_3} \tag{22}$$

$$a_3 = \frac{\mu_c N_1^2 A_1}{g R_1} \tag{23}$$

$$b = \left(\frac{1}{R_1} + \frac{1}{R_3}\right) \frac{\mu_0 N_1^2 A_1 A_3}{g (A_1 + A_3)} \tag{24}$$

and

$$\bar{G}_{10} = -\frac{2 N_1 A_1}{N (A_1 + A_3)} \tag{25}$$

$$\bar{G}_{20} = -\frac{2 N_1}{N} \tag{26}$$

$$\bar{G}_{30} = -\frac{2 N_1 A_3}{N (A_1 + A_3)} \tag{27}$$

It follows immediately from (19) through (21) that $\bar{G}_{10}$, $\bar{G}_{20}$, $\bar{G}_{30}$, are the low frequency gains of the sensor obtained by letting ω approach zero. The high-frequency gains are similarly obtained by letting ω approach infinity, giving

$$\bar{G}_{1\infty} = \frac{a_1}{b}\bar{G}_{10} = -\frac{2N_1R_1}{N(R_1 + R_3)} \tag{28}$$

$$\bar{G}_{2\infty} = \bar{G}_{20} = -\frac{2N_1}{N} \tag{29}$$

$$\bar{G}_{3\infty} = \frac{a_3}{b}\bar{G}_{30} = -\frac{2N_1R_3}{N(R_1 + R_3)} \tag{30}$$

The maximum low-frequency gain of a given sensor output occurs when the area of adjacent stator teeth opposite the rotor pole piece is zero, giving

$$\bar{G}_{0\,max} = -\frac{2N_1}{N} \tag{31}$$

The magnitude of low-frequency gain, G_0, varies between

$$0 < G_0 < \frac{2N_1}{N} \tag{32}$$

The range of variation in low frequency gain is the same for each output so that no distinction is required between outputs and the first subscript is dropped. For equal resistive loading on each output $R_1 = R_2$ and the high-frequency gain is

$$\bar{G}_\infty = -\frac{N_1}{N} \tag{33}$$

which is one-half of the maximum low-frequency gain. The normalized sensor gain for output 1, $\bar{G}_{n1}$, as a function of the normalized angular frequency, ω_n, is given by

$$\bar{G}_{n1} = \frac{1 + j\alpha\omega_n}{1 + j\beta\omega_n} \bar{G}_{n10} \tag{34}$$

where

$$\bar{G}_{n1} = \frac{\bar{G}_1}{\bar{G}_{0\,max}} \tag{35}$$

$$\bar{G}_{n10} = \frac{A_1}{A_1 + A_3} \tag{36}$$

$$\omega_n = \frac{\mu_0 N_1^2 A_2}{g R_3} \omega \tag{37}$$

$$\alpha = \frac{A_3}{A_2} \tag{38}$$

$$\beta = \left(1 + \frac{R_3}{R_1}\right) \frac{A_1 A_3}{A_2 (A_1 + A_3)} \tag{39}$$

Bode plots of the normalized gain magnitude for equal resistive loads, R, on each sensor output are given in Figure 17. Then

$$\frac{\beta}{\alpha} = \frac{2A_1}{A_1 + A_3} = 2\,G_{n10} \tag{40}$$

and

$$G_{n1} = \left[\frac{1 + (\alpha \omega_n)^2}{1 + 4G_{n10}^2 (\alpha \omega_n)^2} \right]^{1/2} G_{n10} \tag{41}$$

The curves of Figure 17 are not limited to a magnetic structure with particular proportions but apply to any sensor structure within the constraints of relation (1). The results apply to any of the sensor outputs where

A_1 = active area of given stator tooth opposite rotor pole piece

A_2 = total stator tooth area

A_3 = active area of adjacent stator tooth opposite rotor pole piece

The normalized sensor bandwidth, BW_n, is defined as the normalized low corner-frequency, and for output 1 is given by

$$BW_{n1} = \frac{1}{\alpha} = \frac{A_2}{A_3}, \quad \text{for } \frac{A_1}{A_3} < 1 \tag{42}$$

$$BW_{n1} = \frac{1}{\beta} = \frac{A_2 (A_1 + A_3)}{2 A_1 A_3}, \quad \text{for } \frac{A_1}{A_3} > 1 \tag{43}$$

These general expressions for the normalized sensor bandwidth are evaluated in four intervals, each covering a range of angular positions of the rotor. For angular positions in which the edges of the rotor pole(s) are on adjacent stator teeth

$$A_1 + A_3 = K A_2 \tag{44}$$

where K is constant and is restricted to the range $0 < K < 2$ by relation (1). The normalized bandwidths in each interval are as follows.

Interval I boundaries are defined by $A_1 = 0$ and $A_1 = (K-1)A_2$, with $A_2 = A_3$ valid throughout the interval. The range of values A_3/A_2 and A_1/A_3 in I are then

$$\frac{A_3}{A_2} = 1 \tag{45}$$

and

$$0 < \frac{A_1}{A_3} < K - 1 \tag{46}$$

where $1 < K < 2$ so that equation (42) applies and

$$BW_{n1} = 1 \tag{47}$$

throughout interval I.

Interval II boundaries are defined by $A_3 = A_2$ and $A_3 = A_1 = KA_2/2$, with equation (44) valid throughout the interval. The range of values A_3/A_2 and A_1/A_3 in II are then

$$\frac{K}{2} < \frac{A_3}{A_2} < 1 \tag{48}$$

and

$$K - 1 < \frac{A_1}{A_3} < 1 \tag{49}$$

where $1 < K < 2$ so that equation (42) applies and

$$BW_{n1} = \frac{A_2}{A_3} \tag{50}$$

throughout interval II.

Interval III(a) boundaries are defined by $A_1 = A_3 = KA_2/2 > A_2/2$ and $A_1 = A_2$, with equation (44) valid throughout the interval. The range of values A_3/A_2 and A_1/A_3 in III(a) are then

$$K - 1 < \frac{A_3}{A_2} < \frac{K}{2} \tag{51}$$

and

$$1 < \frac{A_1}{A_3} < \frac{1}{K - 1} \tag{52}$$

where $1 < K < 2$ so that equation (43) applies and

$$BW_{r1} = \frac{K}{2\left(\frac{A_3}{A_2}\right)\left(K - \frac{A_3}{A_2}\right)} \tag{53}$$

throughout interval III(a).

Interval III(b) boundaries are defined by $A_1 = A_3 = KA_2/2 < A_2/2$ and $A_3 = 0$, with equation (44) valid throughout the interval. The range of values A_3/A_2 and A_1/A_3 are now

$$0 < \frac{A_3}{A_2} < \frac{K}{2} \tag{54}$$

and

$$1 < \frac{A_1}{A_3} < \infty \tag{55}$$

where $0 < K < 1$, and equation (53) still applies.

Interval IV boundaries are defined by $A_3 = (K-1)A_2$ and $A_3 = 0$, with $A_1 = A_2$ valid throughout the interval. The range of values A_3/A_2 and A_1/A_3 are then

$$0 < \frac{A_3}{A_2} < K - 1 \tag{56}$$

and

$$0 < \frac{1}{K-1} < \frac{A_1}{A_3} \tag{57}$$

so that equation (43) applies and

$$BW_{n1} = \frac{1 + \frac{A_3}{A_2}}{2\left(\frac{A_3}{A_2}\right)} \tag{58}$$

The normalized sensor bandwidth is independent of A_1 throughout interval IV.

A plot of the normalized sensor bandwidth for output 1, BW_{n1}, as a function of the fractional active area on the adjacent stator tooth, A_3/A_2, is given in Figure 18. It is readily seen from the figure that BW_{n1} is a monotonically decreasing function of A_3/A_2 so that the minimum normalized bandwith of the sensor, BW_{nm}, for all angular positions of the rotor is

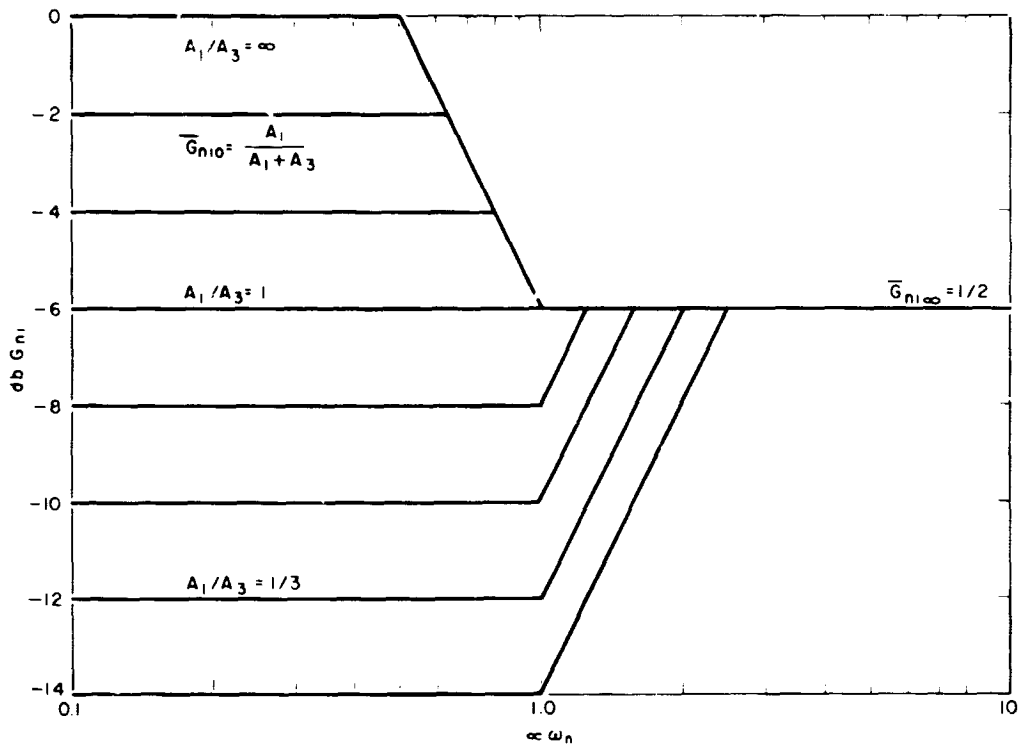

Figure 17–Bode Plots of Normalized Sensor Gain (modified frequency scale)

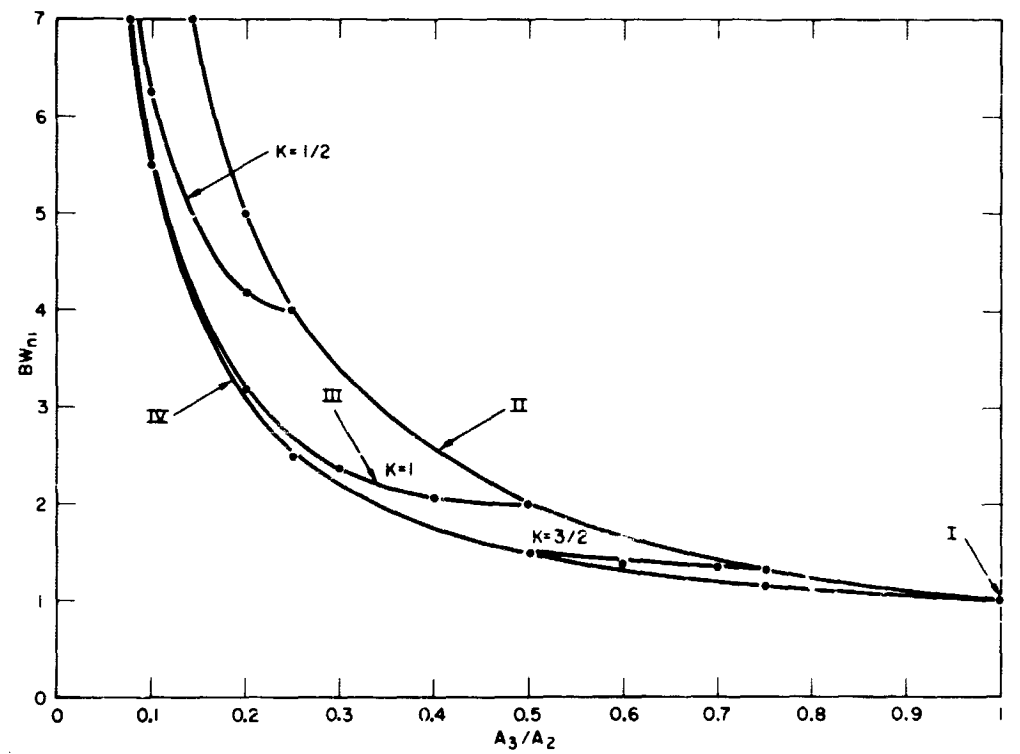

Figure 18–Normalized Sensor Bandwidth vs Fractional Active Area on Adjacent Stator Tooth

$$BW_{nm} = \frac{A_2}{A_3}\Bigg|_{A_1 \to 0} \tag{59}$$

The minimum normalized bandwidth is thus equal to the reciprocal of fractional active area on the adjacent stator tooth as minimum output is approached.

The sensor input impedance, $\bar{Z}$, at maximum gain and for equal resistive loading on each output is obtained from equation (18) by setting $R_1 = R_2 = R_3 = R$, and $A_3 = 0$, and combining with (37) to give

$$\left[\left(1 + \frac{A_2}{A_1}\right) + 2j\omega_n\right]\bar{E}_{in} = \frac{j\omega_n R}{4}\left(\frac{N}{N_1}\right)^2 \bar{I}_{in}$$

Thus the input impedance at maximum gain is maximum for $A_1 = A_2$, and at low frequencies approaches

$$\bar{Z}_{0\,max} = \frac{j\omega_n R}{8}\left(\frac{N}{N_1}\right)^2 \tag{60}$$

The normalized input impedance of the sensor for rotor positions corresponding to minimum normalized bandwidth and equal resistive loading on each output is obtained from equation (18) by setting $R_1 = R_2 = R_3 = R$, and $A_1 = 0$, and combining with (37), (59), and (60) to give

$$\bar{Z}_{nm} = \frac{\bar{Z}_m}{\bar{Z}_{0\,max}} = \frac{2}{1 + BW_{nm} + 2j\omega_n} \tag{61}$$

where the normalization is with respect to $\bar{Z}_{0\,max}$. It is thus seen that the normalized sensor input impedance at minimum output approaches zero for a sensor design in which the minimum normalized bandwidth is made indefinitely large.

The active area of stator teeth 1 and 3 are related to the rotor angular position, θ, by

$$A_1 = K_1 \theta + K_2 \tag{62}$$

$$A_3 = K_3 \theta + K_4 \tag{63}$$

where K_1, K_2, K_3, K_4 are constants, and are positive, negative or zero depending on the angular interval considered. Substituting (62) and (63) into (36) we get

$$\overline{G}_{n10} = \frac{K_1 \theta + K_2}{(K_1 + K_3) \theta + K_2 + K_4} \tag{64}$$

from which it is seen that the normalized low-frequency gain is in general a nonlinear function of the rotor angular position, θ. For a sensor geometry that is constrained by (1) we get $K_1 = -K_3 \neq 0$ for some finite interval of θ so that (63) becomes

$$\overline{G}_{n10} = \frac{K_1 \theta + K_2}{K_2 + K_4} \tag{65}$$

and the sensor gain is linearly related to the rotor position in that interval. The linear transition interval over which (65) applies is maximum for a sensor geometry in which

$$W = S + T \tag{66}$$

Then, for $A_1 = 0$, $A_3 = A_2$, at $\theta = 0$, $A_1 = A_2$, $A_3 = 0$ at $\theta = T$, we get from (62) and (63) that $K_1 = A_2/T$, $K_2 = 0$, $K_3 = -A_2/T$, $K_4 = A_2$. Equation (64) for the normalized low-frequency gain of the sensor becomes

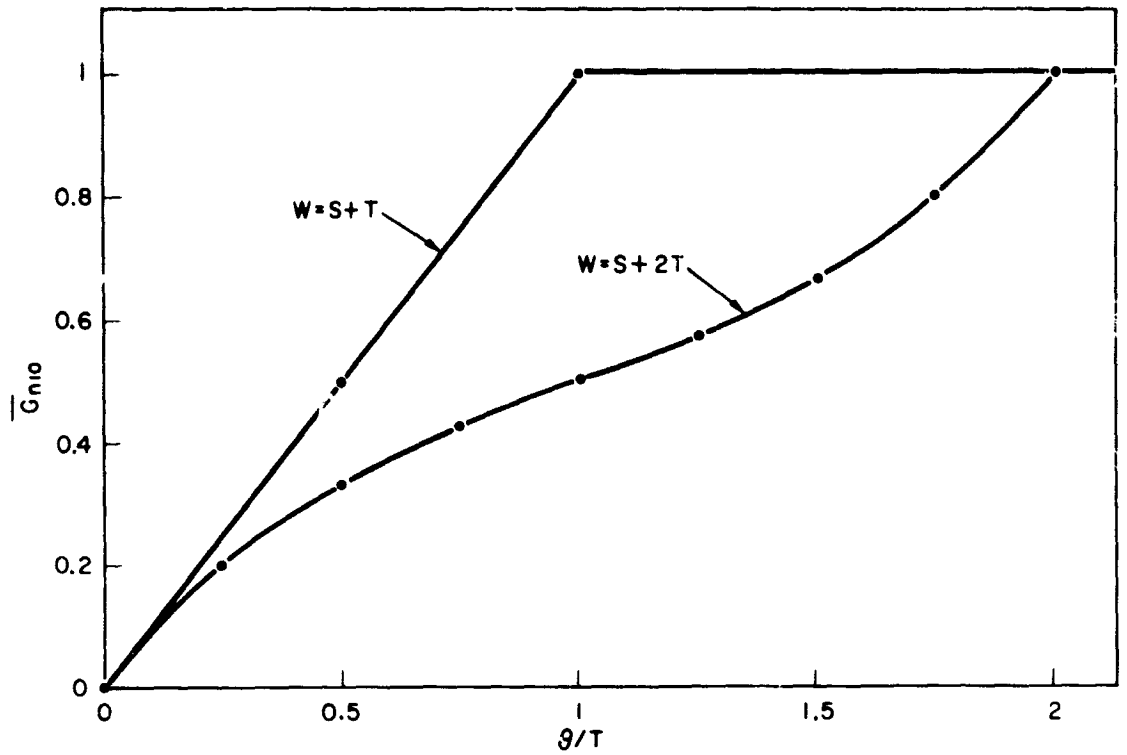

Figure 19–Normalized Low-Frequency Gain vs Rotor Angular Position in Transition Interval

$$\bar{G}_{n10} = \left(\frac{\theta}{T}\right), \quad 0 < \frac{\theta}{T} < 1 \tag{67}$$

The transition from minimum to maximum output is linear for all geometries $W < S + T$ and is nonlinear for $W > S + T$. The normalized low-frequency gain for $W = S + 2T$ is

$$\bar{G}_{n10} = \frac{\left(\frac{\theta}{T}\right)}{\left(\frac{\theta}{T}\right) + 1}, \quad 0 < \frac{\theta}{T} < 1 \tag{68a}$$

$$\bar{G}_{n10} = \frac{1}{-\left(\frac{\theta}{T}\right) + 3}, \quad 1 < \frac{\theta}{T} < 2 \tag{68b}$$

A plot of equations (67) and (68) is given in Figure 19.

REFERENCES

1. Design and Development of a Brushless DC Torque Motor for Use in Solar Array Orientation Systems, NASA Contract NAS5-3934, dated 25 June 1964

2. Design and Development of a Non-Dissipative Charge Controller Using a Rotary Power Transformer, NASA Contract NAS5-9204, dated 17 June 1965

3. Digital Computer Design Fundamentals, Y. Chu, McGraw-Hill, 1962

4. Pulse and Digital Circuits, Millman and Taub, McGraw-Hill, 1956

5. Electromagnetics, J. D. Kraus, McGraw-Hill, 1953